

On the Origin of Interannual and Irregular Behavior in the El Niño

David Strozzi

Department of Physics,

Princeton University

April 26, 1999

Submitted in partial fulfillment of the requirements for the Degree of Bachelor of Arts at
Princeton University.

Abstract

This thesis explores chaotic behavior and response to variations of atmospheric winds in several simple models of the El Niño. We first analyze a three-variable ODE system that possesses intrinsic chaos, and reproduce El Niño behavior by including a background easterly wind. We also see that El Niño event onset is partly locked to an explicit seasonal cycle, and that stochastic forcing in the wind field does not alter the model's qualitative features. We then examine a more complete ocean model based on the shallow-water equations, with a parametrized atmosphere acting as a surface stress. We couple a seasonal wind and Walker circulation to the ocean via a switched mechanism (SFM) and a also a more realistic continuous one (CTM), where the Walker wind strength is determined by the eastern thermocline depth. Both of these systems produce interannual oscillations but seem to become periodic. Using a nonuniform background wind stress, the CTM still has some irregularity after a long time, especially in the height of warm peaks. Analyzing El Niño events in this system reveals strong coupling of onset time to the seasonal cycle and a tendency for strong events to be followed by longer calm stretches. Wind noise is then added to both models, showing that the SFM is extremely sensitive to small changes in the eastern thermocline near the critical value which controls the switch. The CTM is not as sensitive, but wind noise can significantly influence the ocean's evolution. Both models retain their basic characteristics in the presence of noise. Finally, we see that the CTM appears to be a driven oscillator with the wind events acting as impulsive forces that produce transients. While the events can have a strong effect on the ocean, this does not appear until at least a year after the event occurs. Wind events are therefore unable to trigger El Niño in the CTM, although they clearly do this in the SFM. These results show that varying the precise nature of the wind stress and the way it is coupled to the ocean can produce drastically different model behavior and sensitivity to wind events. In particular, the relation of the Walker circulation to the eastern thermocline El Niño governs whether events can bring about an El Niño.

Acknowledgements

Countless people bear part of the responsibility for this thesis, some of whom must unfortunately remain nameless. My parents have not only been completely supportive of me throughout my life, but have also wisely never revealed any preference about what theses I chose to defend. I thank my advisor, Dr. Geoffrey Vallis, for his encouraging me to explore what I found interesting, his flexibility, and his tolerance of my nagging. Most of what I know about dynamical systems I owe to Dr. Philip Holmes, who also made constructive suggestions on the work presented in Chap. 2. This chapter is partly based on a paper written for the MAE 571 class he taught in the Fall 1998 semester. Ron Pacanowski greatly helped this project by sharing his FORTRAN shallow-water model code and substantial expertise in numerical simulation with me. On a similar note, I apologize to my ~~Intel~~ AMD-Inside computer for the 2^N bits, adds, multiplies, and occasional full C: drive. Matt Harrison provided useful insight regarding Westerly Wind Events. Martin Kemp and Dilum Ranatunga were invaluable sources of C++ lore. My other friends and roommates would doubtlessly take issue with me if I failed to mention how important they have been to me, and how much lighter a burden they have made this thesis. I should also thank my countrymen; the politics of recent history has provided a constant source of amusement, heated conversation, and procrastination, if not inspiration.

Dedicated to Maryann Behr, who switched me from the irregular state of wanting to President of the United States.

Cast of Characters

The following acronyms are used throughout this thesis, and are defined on the page cited.

AED: Average η Difference (p. 39)

CTM: Continuous Tanh Model (p. 33)

ODE: Ordinary Differential Equation

PDE: Partial Differential Equation

SFM: Switched Forcing Model (p. 28)

SST: Sea Surface Temperature (p. 1)

SWM: Shallow-Water Model (p. 21)

WWE: Westerly Wind Event (p. 42)

This thesis represents my own work, written in accordance with University regulations.

David Strozzi

April 26, 1999

Contents

1	Overview of ENSO	1
2	A Simple Chaotic Model	6
2.1	The Basic Model	6
2.2	The Background Surface Wind x^*	10
2.3	Effects of Seasonal Cycle	14
2.4	Stochastic Forcing	19
3	Forced Shallow-Water Models	21
3.1	The Shallow-Water Model	21
3.2	Wave Dynamics	25
3.3	A Switched Forcing Mechanism (SFM)	26
3.4	A More Realistic Forcing Function (CTM)	32
4	Noise and Westerly Wind Events	37
4.1	Stochastic Noise in the Wind Field	37
4.2	Effects of Westerly Wind Events	42
5	Conclusions and Future Prospects	47

Chapter 1

Overview of ENSO

Although the climate phenomenon known as El Niño has become a topic of heavy scientific, commercial, and popular interest in recent years, it has been an important part of human life for centuries. The term initially referred to abnormally warm waters flowing southward along the Peruvian coast around the Christmas season. The devout inhabitants of the region dubbed these warm currents “El Niño” (Spanish for “the Boy”), in reference to the Christ child. Such currents appear annually, but about every 2 to 4 years the amount of warm water is much larger than during a typical year. These anomalous currents inflict great damage to the fish and plankton populations off the Peruvian coast, and have a devastating impact on the local economy. Among scientists, the term El Niño is reserved for these irregular events and associated geophysical phenomena. The earliest record of an El Niño dates from Francisco Pizarro’s campaign logs of 1525-1526, where unusually abundant conditions in Peru’s deserts caused by the event may have allowed him to invade Cuzco.

Understanding of the El Niño was greatly advanced when Berlage in 1957 noticed that sea surface temperatures (SSTs) along the Peruvian coast are correlated with an atmospheric phenomenon called the Southern Oscillation (SO). An important feature of the tropical Pacific is the tendency for low surface atmospheric pressures and rising air in the west (around Indonesia) to be matched with high pressure and sinking air in the southeast. This pressure gradient, along with the vanishing of the wind-field divergence in order to conserve mass, drive the dominant easterly (westward-blowing) surface trade winds. This system is known as the Walker circulation. The SO refers to the negative correlation between changes in western and eastern air pressures; that is, an

increase in one is generally simultaneous with a decrease in the other. It is now well established that the appearance of high pressures in the west is strongly coupled to the onset of El Niño events.

Bjerknes in the 1960s attempted to explain this correlation through a coupled ocean-atmosphere model. A highly productive way to look at the tropical ocean is as consisting of two layers, a warm, shallow surface layer on top of a cold, deep abyss. Temperature changes rapidly at the thin interface between the two, called the thermocline. Atmospheric winds clearly act as a body force on the ocean surface and can drive surface currents. The usually-westward trades therefore tend to move warm surface water to the western Pacific. This depresses the thermocline in the west and elevates it in the east, leading to the tendency for the Pacific to be warmer in the west than east. Consider, however, a decrease in the westward trades. This will allow some surface water to flow eastward, thereby depressing the eastern thermocline and raising the SST. The convective tendency of warm air to rise must be balanced by a horizontal convergence of winds to maintain zero total divergence. The trades will therefore blow more to the east, and we have positive feedback between the tropical ocean and atmosphere which allows disturbances to grow. The high western pressure corresponds to the self-amplifying westerly surface winds, thereby connecting El Niño with the SO. This rough sketch of Bjerknes' basic ideas captures in broad strokes our current picture of the mechanism driving El Niño. Since it involves a Pacific-wide change in the trade winds, it relates the local El Niño along the Peruvian coast with larger-scale geophysics.

Over the last few decades, the theory of El Niño has been significantly fleshed out. It is widely accepted that the phenomenon depends essentially on ocean-atmosphere interactions, and the El Niño-Southern Oscillation ensemble is frequently referred to simply as ENSO. In addition, the older view that El Niño events are anomalies occurring against a backdrop of typical conditions has been abandoned. Philander has advanced the idea that the warm periods are part of an asymmetric cycle with resonant periods, and has named the cool periods La Niña [15]. Our current refined understanding of ENSO has benefited from the fairly complete hierarchy of models of varying complexity, ranging from simple ODE models to full-blown general circulation models (GCMs). It is particularly notable that intermediate coupled models (ICMs), which are not much more sophisticated than the model presented in Chap. 3, seem to outperform the GCMs in predicting El Niño. This suggests that simple physics lies at the core of the phenomenon.

The relation between ENSO and the annual cycle is fundamental but not completely understood.

The seasonal cycle is responsible for switching the ocean between its warm and cold states in many models, such as [1] (discussed at length in Chap. 3). Others, including the celebrated Cane and Zebiak model [4], treat El Niño as a perturbation to the time-averaged annual cycle. It is also well-known empirically that the onset of El Niño is strongly phase-locked to the time of year, with events usually starting when the easterly trades are near the annual minimum. This relationship can be reproduced by even some of the simplest models, and is present in the systems examined below. The seasonal cycle is also one of the dominant time scales in the problem, and a major area of El Niño research has been to determine why the period between observed oscillations is interannual as opposed to yearly. An important theoretical advance in this regard was the delayed oscillator models, the essential ideas of which were presented in terms of an ODE system in [21]. The nonlinear system studied there is:

$$\frac{dT}{dt} = T - T^3 - \alpha T(t - \delta). \quad (1.1)$$

This system can produce oscillations separated by several times the delay δ , depending on the parameter regime.

Linked with wave phenomena, the delayed oscillator is able to partly account for the El Niño time scale in ICM simulations. The main processes which connect conditions in different regions of the Pacific are Kelvin and Rossby waves in the ocean (defined in Chap. 3). Near the equator, fast eastward-moving Kelvin waves are reflected as slow, westward-moving Rossby waves, which are then reflected back eastward as Kelvin waves. It is through this cycle that the ocean provides the “memory” in the system of past atmospheric wind stress. Taking δ to be wave transit times, it is possible to get 2-4 year periods via the multiplying scheme of the delayed oscillator. Models of the El Niño are now sophisticated enough that events can be predicted 6 to 9 months in advance. There is furthermore some understanding of the connection between ENSO and other climatic irregularities throughout the world, such as weaker summer monsoons in India and severe winters in the eastern United States. Such large-scale couplings are called teleconnections and appear to be fairly common. As a result, long-term weather prediction routinely takes them into account.

Certain mathematical aspects of El Niño models have been of particular “pure” scientific interest. First, the system occurs at irregular intervals usually ranging from 2 to 5, but sometimes

as much as 10, years. This raises the question of whether events result from chaos inherent in the large-scale dynamics or from stochastic forcing. Further support for the chaos viewpoint comes from other aspects of the El Niño: events occur quasi-periodically, each event seems to be unique from others, and they display self-similarity (i.e., smaller-scale phenomena resemble the large-scale event). The leading chaos hypothesis is that the ENSO mode interacts nonlinearly with the seasonal cycle in the coupled ocean-atmosphere system. This has been observed in a number of ICMs, where the system follows either the quasi-periodic or period-doubling route to chaos. However, the parameter ranges over which many sophisticated models are chaotic are relatively small. In the stable or periodic regimes, El Niño oscillation can be produced with stochastic forcing added via weather “noise” in the atmosphere. Realistic noise of this type seems able to produce behavior that is generally consistent with observation.

Another important issue is the predictability of El Niño onset. In particular, how far in advance can an event be predicted? Chaos and stochastic forcing both obviously limit forecasting abilities. Much work is currently underway to study how sensitive different models are to perturbation of initial conditions and random forcing. Many believe that it is possible with measured data of reasonable precision to predict events 1 to 2 years in advance, but not much beyond that. Another topic of recent interest in El Niño prediction is the role of westerly wind events in the western Pacific. There is some correlation between their occurrence and the Southern Oscillation, leading some to think that disturbances they generate in the western Pacific can propagate eastward and promote El Niño. The introduction to ENSO presented here draws largely on the review articles [6] and [13]. The former discusses the scientific and more general history of the phenomenon, while the latter outlines extensively the development of ENSO theory.

In this study, we first examine a low-order chaotic model for El Niño developed by Vallis [22]. We see that a background westward wind causes this system to favor a cold eastern ocean, with occasional El Niño events (excursions to a warm state at aperiodic, interannual intervals). As in nature, event onset time is coupled to the seasonal cycle. Although even tiny stochastic wind variations perturb solutions significantly, the basic character of the model is robust to large noise. We then consider a more detailed ocean model based on the shallow water equations with parametrized atmospheric forcing. We demonstrate that a simple switched forcing (the SFM) produces interannual oscillations, and that the eastern ocean tends to be cold when a background

westward wind is added. This model does not produce irregular oscillations, and we modify it with a continuous wind-ocean coupling function (the CTM) that leads to more varied behavior. This model is aperiodic in the presence of a background wind stress that gradually dies off with distance from the equator, while it becomes periodic for a step-function wind. While fairly small wind noise is able to switch the forcing and therefore change the large-scale ocean state in the SFM, the continuous one is less sensitive to noise. Nonetheless, stochastic winds of reasonable strength are still able to change the ocean's state in this model given enough time. We close by considering the effects of western wind events on this model. Wind events clearly throw the SFM into an El Niño state shortly after occurring, but they have little immediate influence on the CTM and do not trigger El Niños in it. In the latter, events act like impulsive forcing to a damped, driven oscillator that generate major transients for several years, perhaps permanently altering the ocean. The models considered here suggest that the wind structure and its coupling to the ocean is a crucial factor in determining how the ocean evolves and responds to wind events, with the ocean being more stable under a less drastic switching of the Walker circulation with eastern thermocline depth.

Chapter 2

A Simple Chaotic Model

In this chapter, we study a chaotic system based on convection and nonlinear advection that represents the large-scale interaction of surface winds with ocean temperature. By choosing parameter values appropriate for the Pacific and including the observed background easterly trade winds, the model behaves similarly to the real El Niño. This demonstrates that chaos internal to the basic large-scale physics may account for such fundamental aspects of the El Niño as aperiodicity, an eastern warm-cold asymmetry, and an interannual time scale. Introducing a seasonal cycle in the parameters phase-locks event onset to time of year, as is known to occur in nature. Even small stochastic forcing of course has a sizeable effect on this chaotic system, but its qualitative El Niño-like behavior is robust to wind noise.

2.1 The Basic Model

Using physical arguments, Vallis motivated a simple, three-parameter model for the eastern equatorial Pacific [22]. In the notation of [23], the model is:

$$\dot{u} = B(T_e - T_w) - C(u - u^*) \quad (2.1a)$$

$$\dot{T}_w = \frac{u}{2\Delta x}(\bar{T} - T_e) - A(T_w - T^*) \quad (2.1b)$$

$$\dot{T}_e = \frac{u}{2\Delta x}(T_w - \bar{T}) - A(T_e - T^*) \quad (2.1c)$$

\dot{f} denotes df/dt . u is the surface wind velocity (positive for eastward flow), and T_e and T_w are

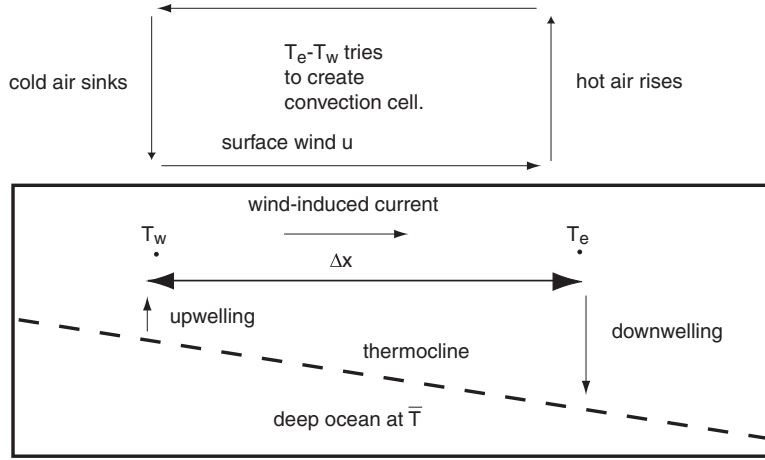


Figure 2.1: Diagram of physical model for $T_e > T_w$.

the water temperature in the eastern and western Pacific, respectively. The temperature difference in Eq. 2.1a stems from the tendency for a convective cell to form (hot air rising, cold air sinking). C reflects wind damping due to friction and other dissipative mechanisms. u^* represents the mean wind flow in the region (which is typically westward, that is, $u^* < 0$). In Eqs. 2.1b-2.1c, the nonlinear $u(T_{e,w} - \bar{T})$ terms account for horizontal advection of water induced by the surface wind, with \bar{T} being the (constant) deep-ocean temperature below the thermocline. T^* is the equilibrium ocean temperature in the absence of wind, determined by balance with heating from above and radiative processes. We can set $\bar{T} = 0$ without changing the problem; this simply shifts the temperature zero-point. Fig. 2.1 contains the model's essential features.

We can consider our three-parameter model as a two-point central-difference discretization in T of the following PDEs:

$$\frac{DT(x,t)}{Dt} = \frac{\partial T}{\partial t} + u \frac{\partial T}{\partial x} = A(T^* - \bar{T}) \quad (2.2)$$

$$\frac{du}{dt} = B(T(l) - T(0)) + C(u^* - u). \quad (2.3)$$

D/Dt denotes the material derivative, so the first equation simply states that T of a fluid parcel changes only due to its difference from the equilibrium T^* . x is the equatorial east-west position. If we imagine incompressible flow along a narrow pipe of length l , then the velocity must be constant throughout by mass conservation, giving $u = u(t)$. As pointed out in [23], the chaos present in our ODE system does not appear if we differentiate Eq. 2.2 with a forward-difference scheme.

Although this model neglects numerous effects (the Earth's rotation, the pressure field, wave phenomena), it is simple enough to be studied analytically and recovers many observed El Niño properties. It is useful to work in unitless variables:

$$\dot{x} = \hat{B}y - \hat{C}(x - x^*) \quad (2.4a)$$

$$\dot{y} = xz - y \quad (2.4b)$$

$$\dot{z} = -xy - (z - 1). \quad (2.4c)$$

$x(x^*)=u(u^*)/(2A\Delta x)$, $y=(T_e - T_w)/2T^*$, $z=(T_e + T_w)/2T^*$, $\hat{B}=T^*B/(\Delta xA^2)$, $\hat{C}=C/A$, and time has been rescaled to At . Notice the close similarity to the Lorenz equations, particularly if we replace our z with $z - 1$ [7]:

$$\dot{x} = \sigma(y - x), \quad \dot{y} = \rho x - y - xz, \quad \dot{z} = -\beta z + xy. \quad (2.5)$$

It is instructive to study the system in the absence of a background wind, $x^*=0$. [7] presents the theory of stability analysis and bifurcations that is used below. Loosely speaking, a bifurcation is a point in parameter space where a system is “structurally unstable,” or small changes in the parameters lead to qualitatively different behavior. It frequently occurs when the stability of fixed points (the sign of their eigenvalues) changes. In what follows, B and C stand for the unitless \hat{B} and \hat{C} . Let us consider the model's behavior as we vary B . The system always has a fixed point at $(x, y, z)=(0, 0, 1) \equiv p_0$, where the eigenvalues of the Jacobian are

$$\lambda_0 = -1, \quad \lambda_{\pm} = -\frac{1}{2} \left(1 + C \pm \sqrt{(C - 2)^2 + 4B} \right). \quad (2.6)$$

λ_0 is always real and negative. λ_{\pm} are always real since the discriminant is nonnegative, and λ_+ is always negative. However, the system bifurcates at $B=C$, where λ_- changes sign and becomes positive for $B > C$. So p_0 is stable for $B < C$ but becomes a saddle with two stable and one unstable eigenvectors for $B > C$. This fixed point corresponds to the fixed origin of the Lorenz system (p_0 is the origin of the $(x, y, z - 1)$ system).

Solving for the other fixed points p_{\pm} , we see that they are complex for $B < C$ and become real

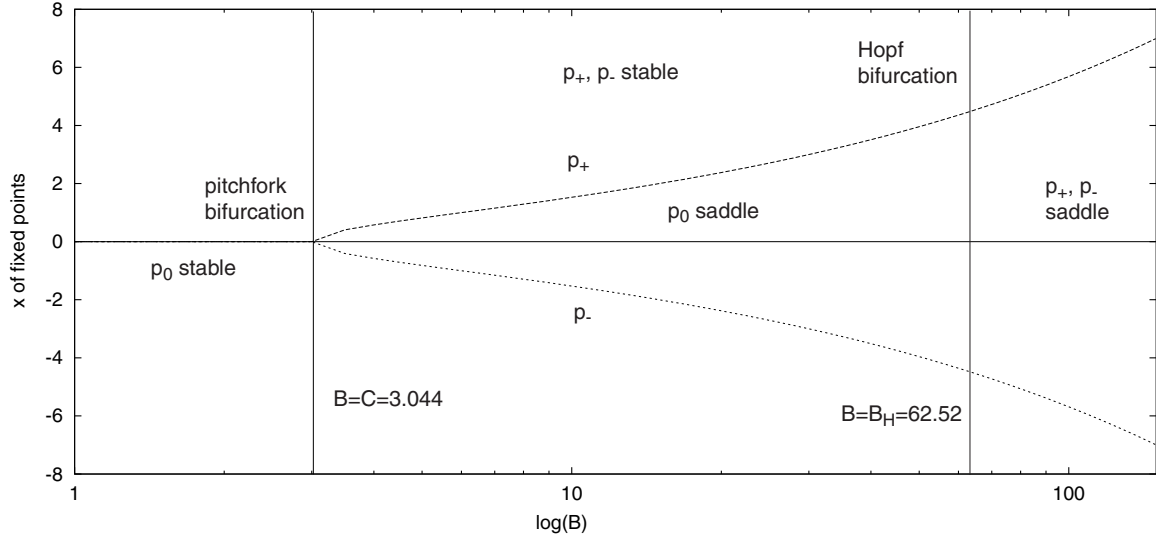


Figure 2.2: Bifurcation diagram for $x^*=0$, $C=3.044$, $B_H=62.52$. B plotted on log scale.

at $B=C$:

$$p_{\pm} = \left(\pm \sqrt{\frac{B}{C} - 1}, \pm \frac{C}{B} \sqrt{\frac{B}{C} - 1}, \frac{C}{B} \right). \quad (2.7)$$

x , y , and z are physical quantities and can only take on real values, so we cannot admit the complex solutions. p_+ represents a point with $x > 0$ and $y > 0$ (i.e., $T_e > T_w$), which corresponds to an El Niño event. The two new fixed points are stable, making $B=C$ a pitchfork bifurcation. We see the emergence of these fixed points just above $B=C$ in Fig. 2.3. However, the system undergoes a Hopf bifurcation at B_H , and all the orbits become unstable. To see this, note that the eigenvalue equation for the Jacobian at either fixed point p_{\pm} is

$$\lambda^3 + \lambda^2(2 + C) + \lambda\left(C + \frac{B}{C}\right) + 2(B - C) = 0. \quad (2.8)$$

It can be shown that the λ 's are complex, with $\text{Re}(\lambda) < 0$ for $B < B_H$ and $\text{Re}(\lambda) > 0$ for $B > B_H$. B_H is the B for which the product of the coefficients of λ^2 and λ equals the constant term, giving

$$B_H = C^2 \frac{C + 4}{C - 2}. \quad (2.9)$$

Fig. 2.2 presents a bifurcation diagram for the $x^*=0$ system. Throughout this study we use physical parameter values $A=1/\text{year}$, physical $C=1/4$ month, $\Delta x=7500$ km, and $T^*=12$ K, which are probably on the right order [23]. B is more troubling to estimate, but let us choose a value

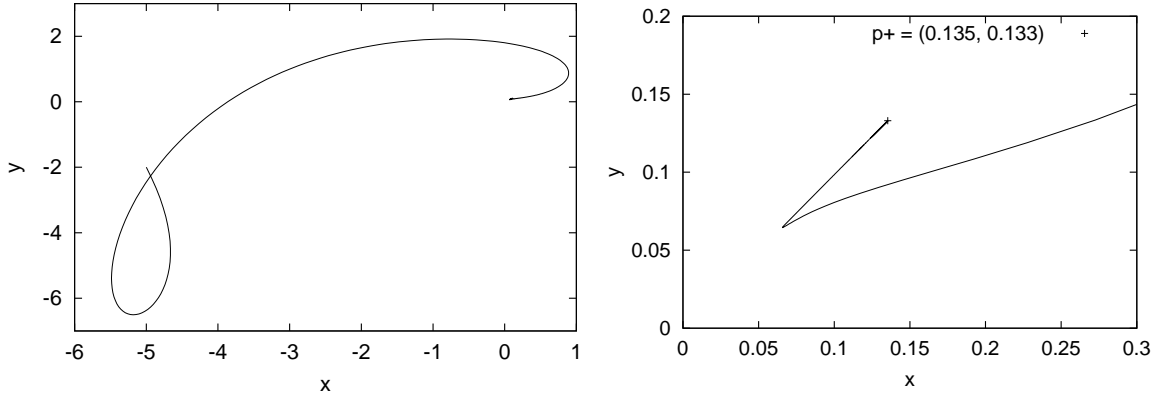


Figure 2.3: Appearance of new stable fixed point when $B=3.1$ in $x^*=0$ system.

that corresponds to physical $B\Delta x \gtrsim 0.6 \text{ m}^2\text{s}^{-2}\text{K}^{-1}$, which gives unitless $B=127$. Note that this is in the unstable regime above $B_H=62.52$. As suggested by the formal similarities to the Lorenz equations, this system contains much of its behavior, including strange attractors and chaos after the Hopf bifurcation. It is well known that in such systems trajectories oscillate between orbiting p_+ and p_- with no set period, as does the El Niño. Fig. 2.4 demonstrates the chaotic nature of the system, and Fig. 2.5 reveals the presence of a strange attractor. Note that the annual time scale for oscillations in this model is set by the frictional damping A and not by an explicitly-imposed seasonal cycle.

2.2 The Background Surface Wind x^*

A major shortcoming of the above $x^*=0$ model is the complete symmetry between T_w and T_e . The real eastern Pacific tends to stay in a state matching p_+ and moves to p_- every several years in an El Niño event. A way to break this symmetry that also agrees with empirical measurements is to introduce a background wind x^* . The trade winds tend to blow westward, which corresponds to $x^* < 0$. With a nonzero x^* , the east-east symmetry cannot be restored by, say, redefining x as $x - x^*$, since this will add new terms to the \dot{y} and \dot{z} equations. Unfortunately, an algebraic treatment of the system also becomes enormously complex with $x^* \neq 0$, since the fixed points are solutions to a cumbersome cubic equation. We can still analyze the system numerically, which reveals a very interesting bifurcation scheme.

First consider the case of x^* small with respect to the natural speeds in the system, say $x^*=-0.021$

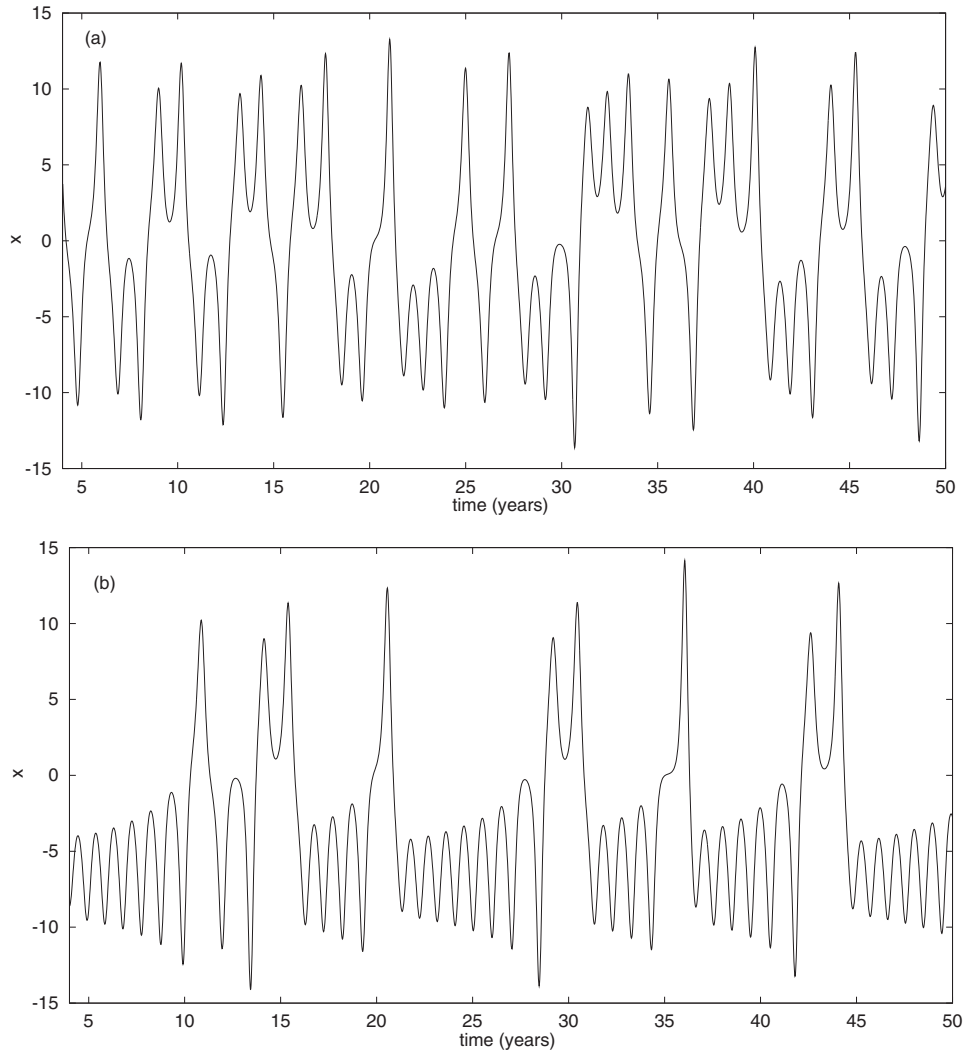


Figure 2.4: x vs. time for $B=127$, (a) $x^*=0$, (b) $x^* = x_0$.

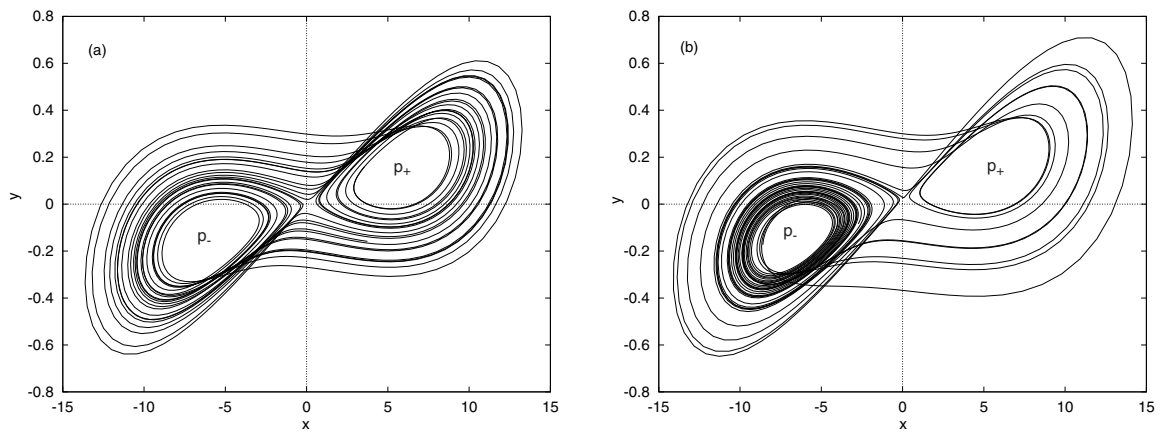


Figure 2.5: Attractors for $B=127$, (a) $x^*=0$, (b) $x^*=x_0$. Integrated for 50 years. System spends more time near p_- when background easterly wind x^* is included.

($u^*=-0.01$ m/s). Fig. 2.6 displays the numerically-computed bifurcation diagrams for $u^*=-0.01$ and -0.45 m/s. The second value is used in [23] as the average westward trade winds, and gives a dimensionless $x^* = 0.95 \equiv x_0$. Note that the fixed point at $x=0$ for small B does *not* stay near $x=0$ as we increase B . Instead, one of the two fixed points formed at the bifurcation approaches $x=0$ but always remains positive. This casts the bifurcation at $B=C$ for $x^*=0$ in a different light. Instead of having a stable fixed point become unstable and two stable fixed points emerge, we have a stable fixed point (p_-) stay stable and move below the x -axis, while a pair of stable and unstable fixed points form. In what follows, we denote the fixed points as indicated in Fig. 2.6b.

We can comprehend this behavior as a codimension two bifurcation at $(0, 0)$ in B, x^* parameter space. The cubic fixed-point equation is

$$(x - x^*)(x^2 + 1) - \frac{B}{C}x = 0. \quad (2.10)$$

When $x^*=0$, we can factor out an x and solve the quadratic equation as before. However, a nonzero x^* leads to a constant term in the cubic equation, breaking the symmetric bifurcation diagram we had above. The same thing happens in the pinned column example discussed in Section 7.1 of [7] when Γ_0 is turned on. In fact, the asymmetric bifurcation diagrams presented there match ours for the $x^* \neq 0$ case (except for stability type). Introducing x^* not only breaks the symmetry between east and west but also moves us away from the codimension two pitchfork to a codimension one bifurcation.

For $x^*=x_0$, the bifurcation where two new fixed points (p_0 and p_+) appear was numerically found to occur at $B=10.635$. However, all three eigenvalues of p_- remain stable for this B , and will stay so until two of them develop positive real parts at $B \sim 101$. As before, p_+ is initially stable, but two of its eigenvalues become unstable at $B \sim 36$. p_0 , on the other hand, is a saddle with two stable and one unstable eigenvalues from its creation at $B = 10.635$ throughout the range investigated. The bifurcations of the $x^* \neq 0$ flow are clearly richer than the $x^*=0$ case, but we still have a point, $B=101$, after which all fixed points are saddles and we have chaotic behavior. For the physical values mentioned above, B will generally be above 127, well within this unstable range. We will nonetheless venture into the stable regime when we add a seasonal variation to T^* and thereby to B as well.

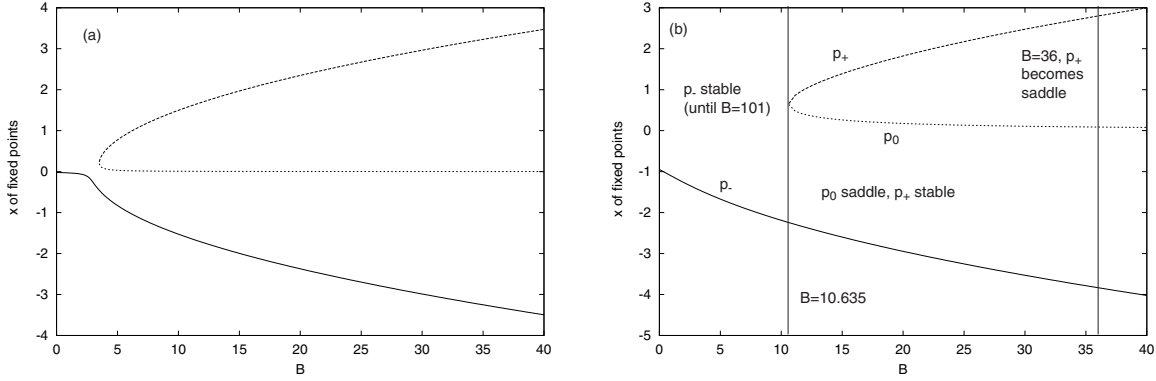


Figure 2.6: Bifurcation diagrams for $B = 127$, (a) $x^* = -0.021$, (b) $x^* = x_0$.

Besides stability analysis, another technique used to study chaos is Lyapunov exponents. One important aspect of chaotic systems is sensitive dependence on initial conditions, that is, the separation between flows launched from nearby points grows exponentially with time. Lyapunov exponents attempt to measure this growth, and are most easily defined for discrete maps. Let $\phi_t(x)$ be the flow with initial condition x that satisfies $\dot{x} = g(x)$. We define the map $f(x) = x + \Delta t g(x)$, which gives $f(x) = \phi_{\Delta t}(x)$ in the limit of small Δt . $f^n(x)$ approximates $\phi_{n\Delta t}(x)$, as in Euler's method for solving differential equations. Suppose we write the difference between the flows launched at x_0 and $x_0 + \epsilon$ after n iterations as $d_n \equiv \epsilon e^{\mu n}$. We know that

$$d_n = \phi_{n\Delta t}(x_0 + \epsilon) - \phi_{n\Delta t}(x_0) \approx f(x_0 + \epsilon) - f(x_0) \approx \epsilon \left. \frac{df}{dx} \right|_{x_0}. \quad (2.11)$$

The Lyapunov exponents are the values which μ approaches for large n :

$$\mu = \lim_{n \rightarrow \infty} \frac{1}{n} \sum_{i=0}^{n-1} \log \left| \frac{df(x_i)}{dx} \right| \quad (2.12)$$

A system with n variables has n Lyapunov exponents. A complete derivation is given in [11]. Exponential growth of initial differences leads to a positive μ . One Lyapunov exponent usually corresponds to the system's fastest-growing instability, so any positive μ is generally taken to imply chaos. Fig. 2.7 shows the Lyapunov exponents for $x^* = 0, x_0$. The appearances of $\mu > 0$ match the bifurcations to unstable fixed points discussed above, confirming the onset of chaos at these values of B . Notice also that each system contains islands of stability past the transition to chaos where no μ is positive.

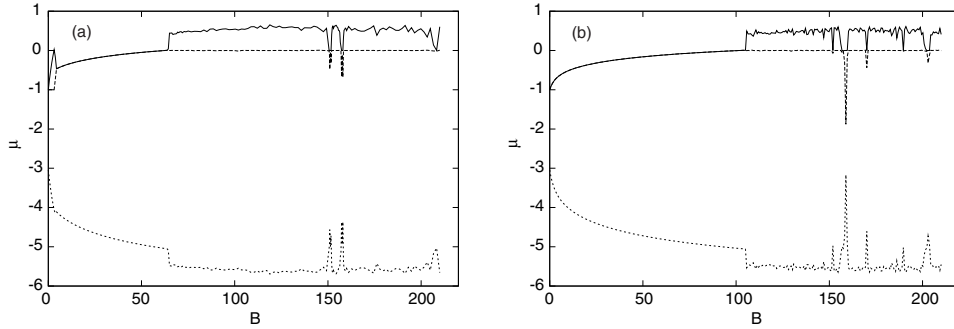


Figure 2.7: Lyapunov exponents for $B=127$, (a) $x^* = 0$, (b) $x^* = x_0$. Appearance of positive exponents indicates chaos and agrees with bifurcation analysis.

With the addition of x^* , the model now replicates the major features of El Niño. Figs. 2.4 and 2.5 show that the system does indeed tend to have a westward surface wind, which corresponds to orbiting p_- preferentially. El Niño events, characterized by motion near p_+ and a positive x , occur every so often with an irregular period. Examining the temperature difference $y \propto T_e - T_w$ over time also reveals anomalously warm eastern waters at the same time that the surface wind x blows eastward. Fig. 2.8 portrays y with and without x^* .

2.3 Effects of Seasonal Cycle

To bring the model further in accordance with reality, let us introduce a seasonal cycle. It is a well-known fact [22] that the onset of El Niño is partially phase-locked to the time of year, with events much more likely to start when the trade winds are weak or eastward as opposed to their westward average. We incorporate this effect by letting x^* vary with time:

$$x^* = x_0(1 + x_s \sin \omega t), \quad (2.13)$$

where x_s is a dimensionless amplitude and $\omega \equiv 2\pi/\text{year}$. As x_s increases, the relative importance of the constant offset x_0 is diminished, and the symmetry between east and west present when $x^*=0$ is somewhat restored. However, one can still make x_s large enough to reverse the trade wind direction ($x_s > 1$) and obtain solutions qualitatively like the El Niño behavior seen above (the system tending to orbit around p_- with brief excursions to p_+). Fig. 2.9 displays the effects of both changing B and adding the seasonal cycle. In particular, notice that increasing B , which

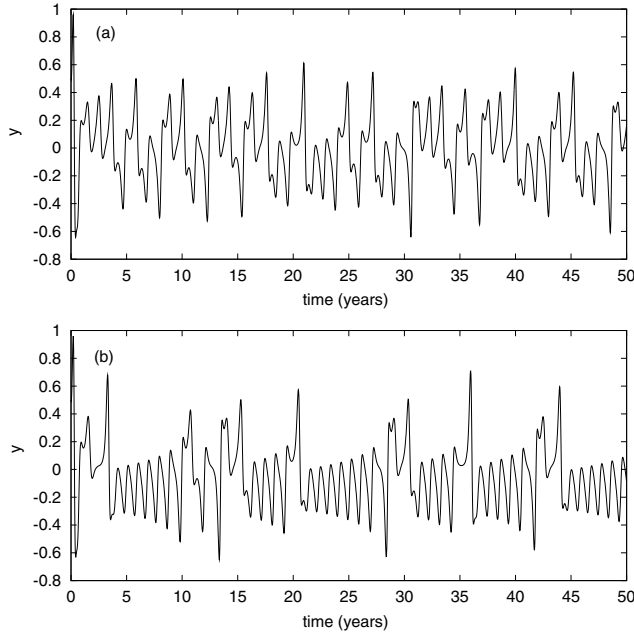


Figure 2.8: Temperature difference y for $B=127$, (a) $x^*=0$, (b) $x^*=x_0$. Spikes in (b) coincide with El Niño events in x , see Fig. 2.4.

controls the coupling between the temperature difference y and the winds x , makes the system move more readily into an El Niño state (the effect is more pronounced for higher B , but I chose 191 since it behaves nicely for large x_s). Furthermore, adding $x_s=3$ causes trajectories to orbit around each fixed point p_{\pm} for a number of years before returning to the other one, eliminating El Niño behavior. Incorporating both effects, however, leads to El Niño (asymmetric) motion.

Having found a physically reasonable set of parameters with the desired solutions, we can now study the correlation between the seasonal cycle and El Niño onset. Fig. 2.11 shows the month of event onset (defined by x becoming positive) during the year. In (a) there is no background coupling to time of year, as we should expect. In agreement with observation, (b) indicates that events tend to start when the trade winds are weak. Also note that the total number of events is almost twice as large in the presence of the seasonal cycle.

Another way to represent the seasonal cycle is by varying the equilibrium ocean temperature T^* rather than x^* . Recall that T^* appears in the rescaled system as -1 in Eq. 2.4c. In addition, the coupling parameter \hat{B} , which determines the stability of fixed points, is proportional to T^* . We therefore expect a small T^* to stabilize the system, that is, inhibit El Niño events by moving us

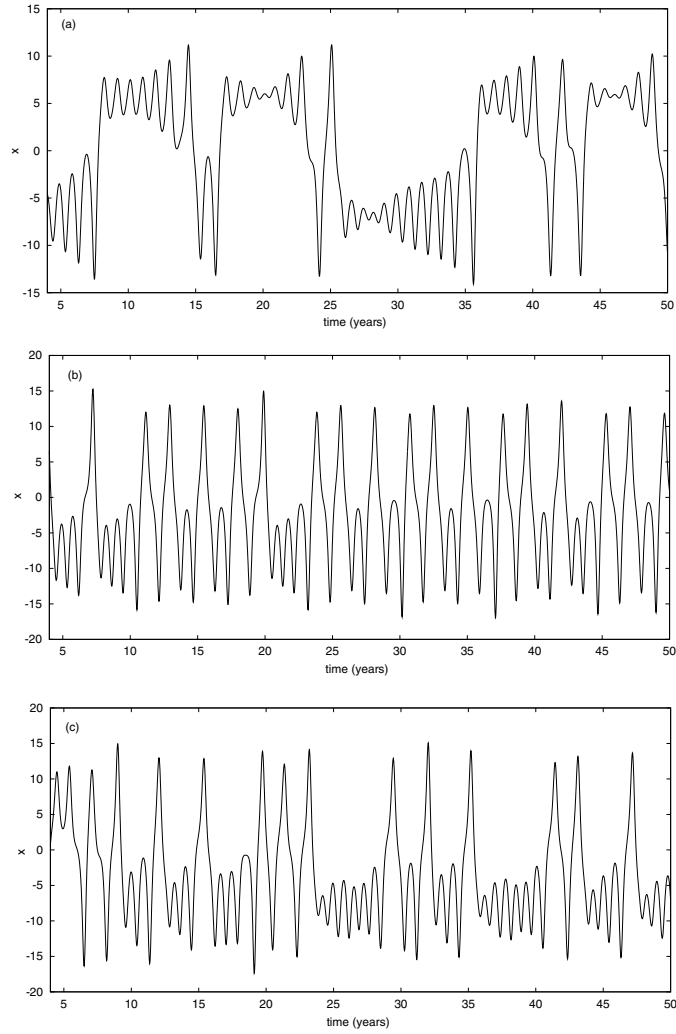


Figure 2.9: Effects of seasonal cycle in x^* and varying B . (a) $B=127$, $x_s=3$, (b) $B=191$, $x_s=0$, (c) $B=191$, $x_s=3$.

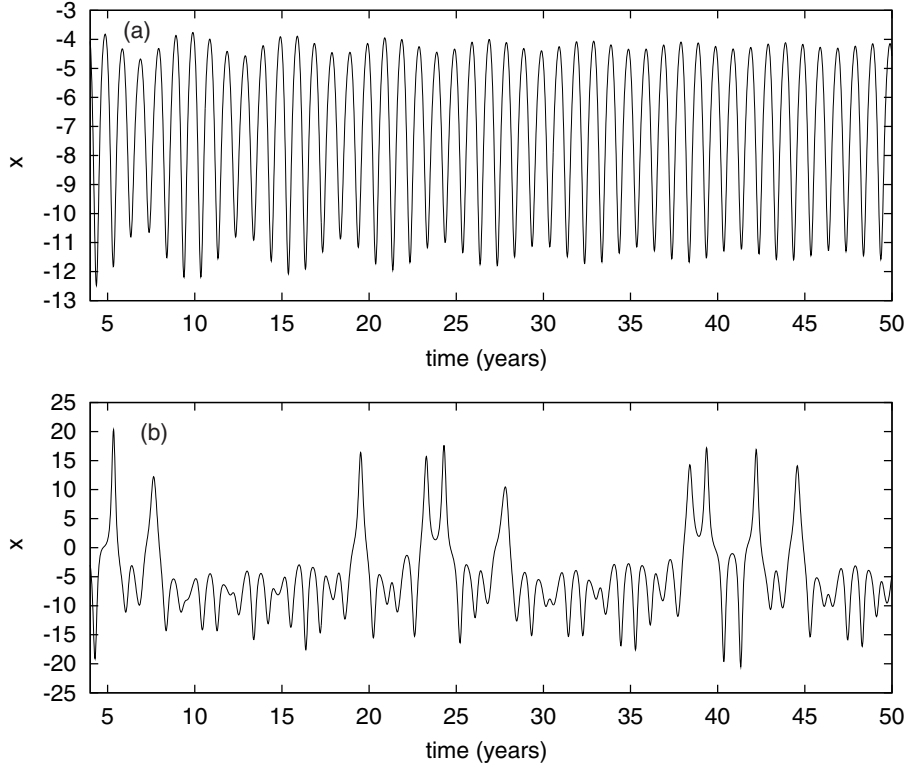


Figure 2.10: Effects of seasonal cycle with $x^*=x_0$, $T_s=0.42$ for (a) $B=127$, (b) $B=191$.

near the stable $B < 101$ regime. We introduce a time-varying T^* as follows:

$$T^* \rightarrow T^*(1 + T_s \sin \omega t), \quad \dot{z} = -xy - (z - 1 - T_s \sin \omega t), \quad \hat{B} = \frac{BT^*(1 + T_s \sin \omega t)}{\Delta x A^2} \quad (2.14)$$

T_s is the dimensionless seasonal cycle amplitude and ω is the annual frequency used above. We leave y and z rescaled only by the constant T^* . T^* represents the average temperature difference between the upper and deep (sub-thermocline) ocean, which we know is always positive (since cold water sinks and the ocean is heated from above). We therefore cannot have $T_s > 1$. Let us choose $T_s=0.42$ as a reasonable value for moderate seasonal variation.

Fig. 2.10a shows the effect of this T_s on our basic case $B=127$. The improved stability when T^* and B are small seems to overcompensate for the instability when they are large: apparently a large B becomes small again before the system “feels” it while orbiting p_- . For $T_s=0.42$, the minimum B is 74, well below the critical $B=101$ where p_- becomes unstable. This counteracts the effect of introducing a seasonal cycle in x^* , which helps restore the east-west symmetry and promotes El Niño events. As before, increasing B moves the system back into El Niño behavior in

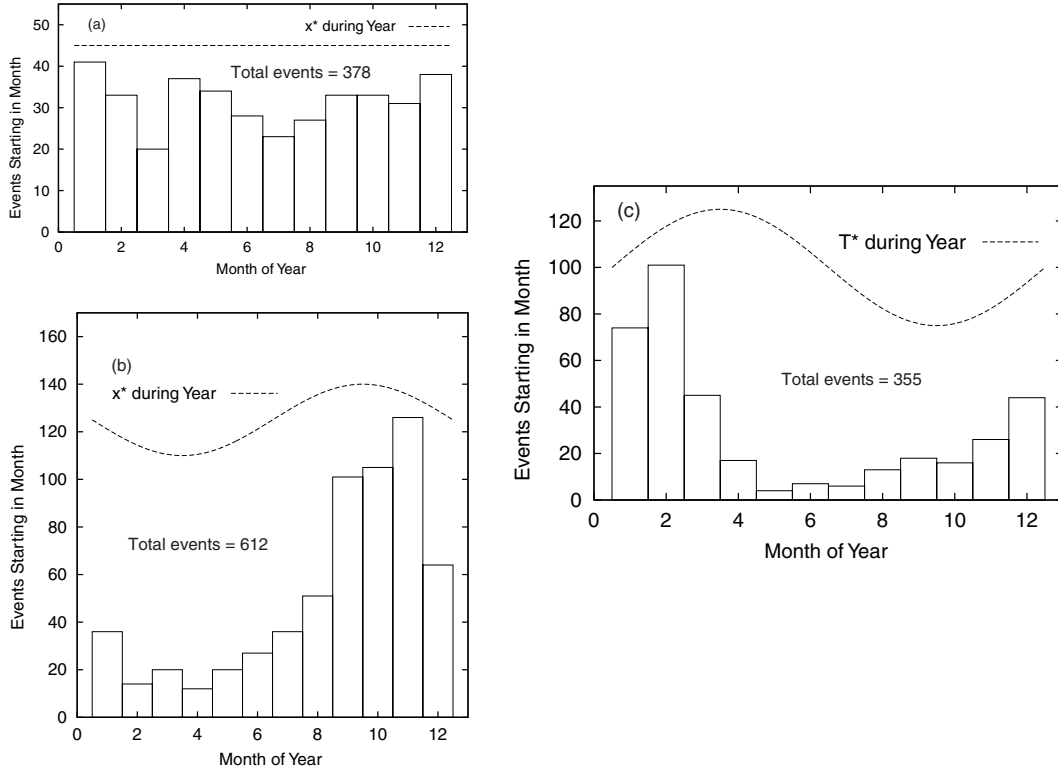


Figure 2.11: Coupling of onset time to seasonal cycle for 2000-year integrations, $B=191$, $x^*=x_0$. (a) $x_s=0$, $T_s=0$, (b) $x_s=3$, $T_s=0$, (c) $x_s=0$, $T_s=0.42$.

Fig. 2.10b. The coupling of event onset time with T^* is displayed in Fig. 2.11c and is somewhat surprising. While there is a quite strong seasonal dependence of onset time, it is out of phase with our intuitive expectations. We would suppose El Niño events occur when T^* is large and the system is unstable, but it seems that they start *before* T^* reaches its maximum. This may be due to a large lagtime (perhaps ~ 1 year) in system response to T^* , as was suggested for the reason why a seasonal cycle with $B=127$ prevents El Niño from happening. Another possible explanation for the phase difference is that T^* couples to z as well as to x . A varying T^* has little overall effect on the total number of events. The run with time-dependent T^* had 355 events, slightly less than the 378 with no seasonal cycle and about half as many as the 612 observed with a varying x^* . The inclusion of seasonal effects in a way that allows for El Niño behavior and gives an annual dependence of event onset time further encourages us that our simple model captures some of the basic physical mechanisms at work.

2.4 Stochastic Forcing

An important test of our model's relation to nature is to study the effects of "noise," the unresolved or excluded physical processes present in nature. One should have in mind here things such as storms, cyclonic activity, and other "random" events that we have no hope of capturing in our 3-variable model. Since the atmosphere has much more stochastic variability than the ocean, we introduce noise just into the surface wind x :

$$\dot{x} = \hat{B}y - \hat{C}(x - x^*) + x_n. \quad (2.15)$$

We can think of this as stochastically varying the value to which x is trying to equilibrate. At time step i , x_{ni} is given by

$$x_{ni} = \lambda x_{ni-1} + r_i A_N \sqrt{(1 - \lambda^2)}. \quad (2.16)$$

r_i is a random number uniformly distributed between -1 and 1, and A_N measures the noise amplitude. λ sets the time scale for the duration of noise events. Since atmospheric disturbances typically persist for a few weeks, let us choose $\lambda=0.74$, so that an initial disturbance will decay by 99% in 15 days if we set $A_N=0$. $\lambda=0$ corresponds to white noise.

Application of stochastic forcing confirms the chaotic nature of the system. Fig. 2.12 shows the difference between x for noiseless and noisy models with $x^*=x_0$ and $B=127$. We see that the solutions drastically diverge from each other even for an $A_N=1\text{E-}9$ which is tiny compared to $Cx_0=2.89$. Although small noise can cause the model to follow a different trajectory, the system's qualitative El Niño-type behavior is very robust to it. As is seen in Fig. 2.13, even for a large A_N of 10, the system oscillates aperiodically between a warm and cold state, preferentially staying cold. The time-averaged magnitude of x_n is 4.71 for $A_N = 10$ and scales linearly with A_N for the smaller values mentioned above. The fact that increasing A_N by several orders of magnitude delays by a much smaller factor the time when the two models differ considerably stems from the system's intrinsic chaos.

The numerical work presented in this chapter was performed with C++ code using double-precision (64-bit) numbers. Integration of ODEs was done with the fourth-order Runge-Kutta method [2]. The time step was of order 3000-4000 secs, which is much smaller than the step sizes

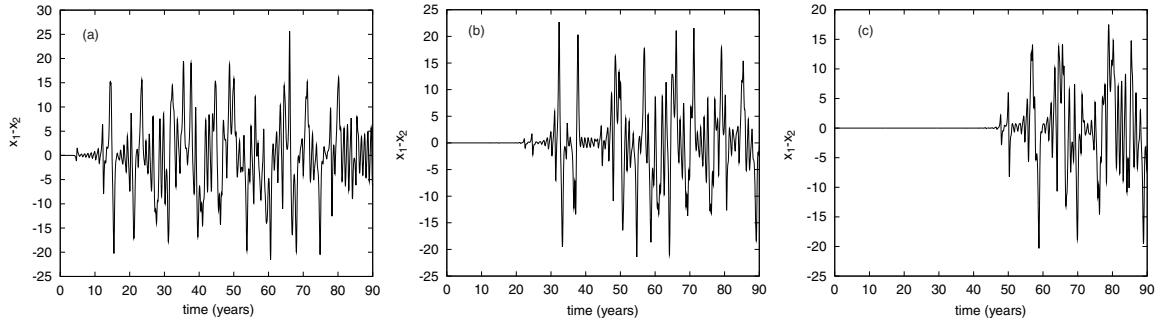


Figure 2.12: x_1-x_2 for x_1 without, x_2 with stochastic noise, $B=127$, $x^*=x_0$. (a) $A_N=0.1$, (b) $A_N=1E-4$, (c) $A_N=1E-9$.

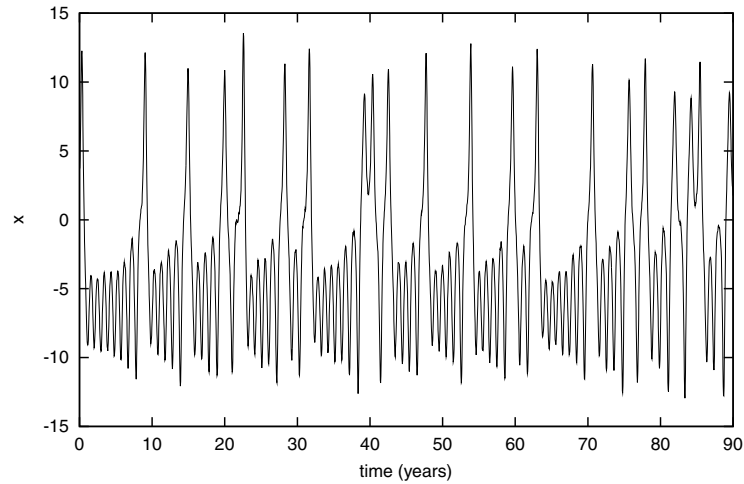


Figure 2.13: $x(t)$ for stochastic noise, $B = 127$, $x^*=x_0$, $A_N=10$. System qualitatively similar to noiseless model.

that gave divergent behavior but still allowed for reasonable execution time. Mathematica v3.0 was used for the numerical fixed point and stability analysis for $x^* \neq 0$. The Lyapunov exponents were calculated using the C package [17]. All random numbers in this thesis were generated with the ran1 algorithm from [18].

Chapter 3

Forced Shallow-Water Models

Having studied a simple, ad hoc ODE model for El Niño, we now proceed to one based on the full-blown equations of geophysical fluid dynamics. We adopt the shallow-water model, a simple and very common system used for thin, homogeneous fluids. Our principle interest is to see how changing the winds and their coupling to the ocean relates to El Niño behavior. We start with wind forcing controlled by a switching mechanism, which produces interannual oscillations between a warm and cold eastern ocean and never equilibrates. Adding a background westward wind keeps the ocean preferentially in the cold state. Unlike the real El Niño, this model is periodic. We modify the ocean-atmosphere coupling to be continuous rather than a step function, and are able to produce variability. A nonuniform westward wind prevents the system from becoming periodic, without resorting to non-deterministic processes such as stochastic noise. In this regime, event onset time is strongly coupled to the seasonal cycle, and, as in nature, strong events tend to be followed by longer periods of calm.

3.1 The Shallow-Water Model

The shallow-water model (SWM) is used extensively in geophysics to study homogeneous (uniform density) fluids whose depth is small compared to the length scale of lateral motions, such as the Pacific ocean. In deriving this model from the primitive fluid dynamics equations, one assumes hydrostatic balance (the pressure field balances gravity) and replaces pressure with height in the

governing equations. This yields

$$\frac{Du}{Dt} - fv + g'\eta_x = \frac{\tau^x}{H} + \nu_h \nabla^2 u - \nu u \quad (3.1a)$$

$$\frac{Dv}{Dt} + fu + g'\eta_y = \frac{\tau^y}{H} + \nu_h \nabla^2 v - \nu v \quad (3.1b)$$

$$\frac{D\eta}{Dt} + H(u_x + v_y) = -\kappa\eta. \quad (3.1c)$$

Coordinate subscripts denote derivatives. x and y refer to the zonal (east-west) and meridional (north-south) directions, and correspond to longitude and latitude coordinates on the Earth's surface. u and v are the ocean currents in the x and y directions, with positive values corresponding to eastward and northward flows, respectively. η represents the perturbation of a fluid column's height from its mean value H . We linearize the η equation by assuming $\eta/H \ll 1$, which may not be justified in light of the magnitude of oscillations seen below. When applied to the ocean, a positive η represents a downward displacement of the lower surface. For a single layer of homogeneous fluid, g' is simply gravitational acceleration g (9.8 m/s²). However, the SWM can be easily adapted to the case of two homogeneous layers of densities ρ_1 and ρ_2 by introducing the reduced gravity

$$g' \equiv \frac{\rho_2 - \rho_1}{\rho_1} g. \quad (3.2)$$

$\tau^{x,y}$ are forcings on the ocean surface, ν_h is the coefficient of viscous dissipation, ν is the coefficient of Rayleigh friction, and κ is the coefficient of Newtonian damping (arising from Newtonian cooling). We treat the Pacific as a warm shallow layer on top of a cold deep abyss with the thermocline separating them. u and v refer to the currents in the upper layer, and η to the thermocline displacement. Table 3.1 lists the values of physical parameters used in this study, and Fig. 3.1 depicts the coordinate system for the SWM.

$f = 2\Omega \sin y$ is the Coriolis parameter and incorporates the Earth's rotation: all quantities are measured with respect to the Earth's surface, which is a rotating, non-inertial frame ($\Omega=2\pi(1/\text{day}+1/\text{year})=2\pi/\text{sidereal day}$). For problems of small meridional extent compared to the Earth's radius, it is customary to expand f in the longitude y :

$$f = 2\Omega(\sin y_0 + y \cos y_0 + \dots) \approx f_0 + \beta y. \quad (3.3)$$

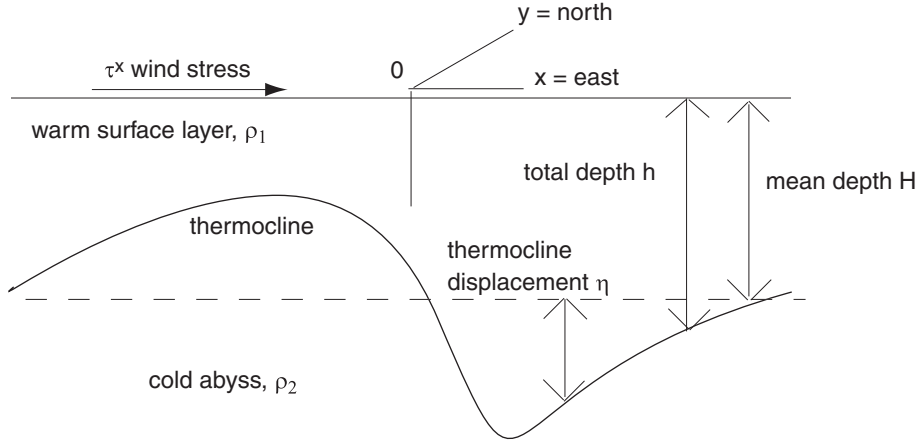


Figure 3.1: Coordinate scheme for two-layer SWM.

parameter	value	parameter	value
L_x	$90^\circ = 10,000 \text{ km}$	g'	0.02 m/s^2
L_y	$80^\circ = 4550 \text{ km}$	H	100 m
dx	$1^\circ \text{ or } 2^\circ$	Ω	$7.29\text{E-}5 \text{ 1/s}$
dy	$1^\circ \text{ or } 2^\circ$	ν_h	$1.5\text{E}4 \text{ m}^2/\text{s}$
dt	1 hour	$\nu = \kappa$	$5\text{E-}9 \text{ 1/s}$

Table 3.1: Values of physical parameters for the SWM.

This is referred to as the “ β -plane” approximation. f is positive (negative) in the northern (southern) hemisphere, but β is always positive. D/Dt is the advective or material derivative (following a fluid parcel), which in fixed spatial coordinates is

$$\frac{Du}{Dt} = \frac{\partial u}{\partial t} + \mathbf{u} \cdot \nabla u \quad (3.4)$$

(\mathbf{u} is the velocity vector). When considering large-scale flows, we are justified in linearizing the equations by neglecting the quadratic advective acceleration terms. Thus, we only keep the linear $\partial u/\partial t$ term in the material derivative. For a detailed discussion of these issues and derivation of the SWM, see [5].

We numerically simulate the SWM with C++ code adapted from a FORTRAN program written by Ron Pacanowski [14]. The code is further discussed and used for the numerical work in [16]. While the model presented above holds on a flat 2-dimensional surface, our simulation incorporates the curvature terms of the full spherical geometry (given in [5], p. 34). In addition, it does not use the β -plane approximation but retains the complete Coriolis parameter f . Derivatives are

computed via a centered finite-difference equation:

$$\frac{\partial f}{\partial x} = \frac{f(x + \frac{h}{2}) - f(x - \frac{h}{2})}{h}. \quad (3.5)$$

For our ocean, we use a rectangular domain of size $0 \leq x \leq L_x$, $-L_y \leq y \leq L_y$. The spatial grid sizes dx , dy and time step dt are chosen to accurately capture the Rossby and Kelvin wave dynamics that are essential to El Niño. We imagine the ocean as bounded by solid walls (the coasts), so the normal velocity components vanish at the edges. However, to compute a function's spatial derivatives at a grid point, we need to know its value at neighboring points. We need up to second derivatives in our system (from $\nabla^2 u$ for viscous damping), which in a centered-difference scheme requires the value at a grid point and its neighbor on each side. Therefore, we ring the ocean with a box where all functions always equal 0, and within that a box where only the normal velocities vanish.

In integrating the SWM numerically, one must choose between a scheme that conserves energy or potential enstrophy (integral of squared vorticity, $\int (v_x - u_y)^2 dV$). A detailed discussion of this issue, as well as two numerical algorithms which differ only in their conservation properties, is given in [20]. We adopt the potential enstrophy-conserving scheme presented there, since this method better replicates the wave dynamics expected from theoretical considerations. In particular, the potential enstrophy-conserving scheme we use captures the stability of large-scale Rossby waves (defined below), while a similar energy-conserving scheme does not [19]. For time derivatives, this method uses the leapfrog (centered-difference) scheme with a Robert time filter [8]. This low-pass filter calculates the time-average \bar{f} of some function $f(t)$ via

$$\bar{f}(t) = f(t) + \gamma [f(t + \Delta t) - 2f(t) + f(t - \Delta t)]. \quad (3.6)$$

The filter severely dampens high-frequency (period $\leq 2\Delta t$) waves, and its effect drops off for lower-frequency components. We choose $\gamma = 0.01$ throughout this study.

3.2 Wave Dynamics

The ocean dynamics fundamental to El Niño are Rossby and Kelvin waves. Consider the unforced SWM with no friction or damping ($\nu_h = \nu = \kappa = 0$). Rossby waves result from the variation of f with latitude y , and are best understood by using the β -plane approximation. A detailed derivation is given in section 6.4 of [5]. The upshot is periodic solutions for the surface displacement of the form $\eta \propto \cos(lx + my + \omega t)$ with the dispersion relation

$$\omega = \frac{-\beta R^2 l}{1 + R^2(l^2 + m^2)}, \quad R \equiv \frac{\sqrt{gH}}{f_0}. \quad (3.7)$$

R is dubbed the Rossby radius of deformation, and l and m are the zonal and meridional wavenumbers. Solving for the zonal phase velocity gives

$$c_x \equiv \frac{\omega}{l} = \frac{-\beta R^2}{1 + R^2(l^2 + m^2)}. \quad (3.8)$$

c_x is always negative, implying Rossby waves can only propagate westward. However, the meridional phase velocity $c_y \equiv \omega/m$ can have either sign.

Unlike Rossby waves, which rely on the Earth's rotation, Kelvin waves only need a lateral boundary to propagate. Along a wall in the y -direction at $x=0$, the zonal velocity $u=0$. Kelvin realized that solutions exist for which $u=0$ everywhere. Following section 6.2 of [5], we can write a wave equation for v :

$$v_{tt} = c^2 v_{yy}, \quad c \equiv \sqrt{g'H}. \quad (3.9)$$

c is the wave's phase velocity. The most general solution for η in the SWM is

$$\eta = \eta_1(y + ct)e^{-x/r} + \eta_2(y - ct)e^{x/r}, \quad (3.10)$$

where η_i is an arbitrary function. Consider a wave travelling in the northern hemisphere ($f > 0$) to the east of a coast ($x > 0$). R is positive, so the η_2 term is unbounded for large x and must be rejected. We see that the amplitude of η_1 decays away from the wall, thereby trapping the wave along a coastline. The wave also propagates southward. We can perform the same analysis for a coastline with arbitrary orientation (and set the normal velocity to 0), so Kelvin waves travel with

the coast to the right in the northern hemisphere and the left in the southern.

Rossby and Kelvin waves appear in altered form near the equator (see Chap. 19 of [5]). Although there are no coastlines, the β -plane approximation near the equator ($f \approx \beta y + \dots$) allows for solutions with $v = 0$ everywhere. The equator thus acts as an effective meridional wall trapping these so-called equatorial Kelvin waves which propagate only to the east at the speed c defined above. Moreover, solutions on the equatorial β -plane exist that strongly resemble Rossby waves. For long wavelengths (small l), the dispersion relation for these waves is

$$c_x \approx \frac{-\beta R_{eq}^2}{2n+1} = \frac{c}{2n+1}, \quad n \geq 1. \quad (3.11)$$

$R_{eq} \equiv \sqrt{c/\beta}$ measures the distance from the equator over which equatorial dynamics dominate midlatitude dynamics. It is now clear that Kelvin waves (phase speed c) travel faster than Rossby waves (phase speed at most $c/5$).

As a first test of our numerical code, let us simulate the evolution of a surface depression with no forcing. The initial ocean has no currents and a surface displacement

$$\eta = \exp [-(x^2 + y^2)/(500\text{km})^2] \text{ m}. \quad (3.12)$$

Fig. 3.2 clearly shows the bulge separating into a fast, east-moving equatorial Kelvin wave and a slower, double-lobed west-moving Rossby wave. This generation of waves is not just caused by disturbances in η but is a quite generic response to wind stress and other perturbations. Once the Kelvin wave reaches the eastern coast, it splits into two Kelvin waves. The simulation agrees with our theoretical expectations of how Kelvin waves travel along a coast in each hemisphere, and also confirms that the equator can be thought of as a meridional boundary.

3.3 A Switched Forcing Mechanism (SFM)

As was discussed in Chap. 1, El Niño relies fundamentally on positive feedback within the coupled ocean-atmosphere system. Therefore, we must somehow incorporate the atmosphere if we are to study El Niño. Although called the SWM, this system is frequently applied to the atmosphere as well as the ocean. One straightforward method is to simulate both an ocean and atmosphere with

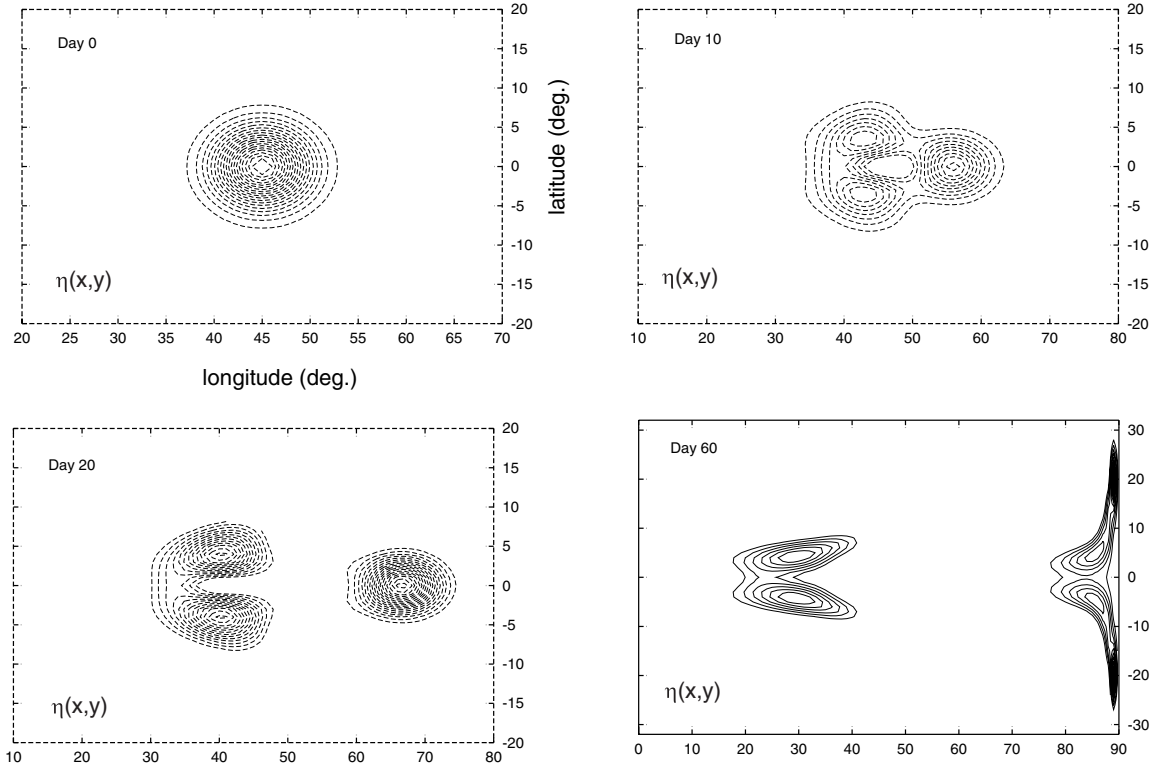


Figure 3.2: Separation of surface depression into Kelvin and Rossby waves in the SWM.

separate SWMs and treat each as an external forcing on the other. In particular, the atmospheric winds act as the body forces $\tau^{x,y}$ which drive ocean currents, and the ocean SST heats the atmosphere (and acts as a source for atmospheric η). This approach was studied in [16], where it was shown that instabilities grow near the equator but not away from it or on a non-rotating Earth. However, [4] points out that the instabilities grow without bound, and that a separate scheme which leads to decay cannot be combined with the one that led to growth. The simulations I performed bear out that equatorial instabilities become arbitrarily large. This behavior persists even if we include the nonlinear advection terms in the primitive equations. While this scheme establishes that the coupled ocean-atmosphere system produces growing instabilities on the equator, it is not useful for our purposes of studying long-term El Niño properties, such as the time between oscillations and relation to the seasonal cycle. We therefore consider a parametrized atmosphere, appearing only as explicit forcings in u and v .

We use the fluid depth η both as a diagnostic of the ocean’s state and to control coupling to the atmosphere. A negative η indicates the thermocline is closer to the surface. The SST roughly

matches the thermocline depth, with a shallow thermocline producing cold surface temperatures. Following [1], we parametrize the atmosphere via the forcings $\tau^{x,y}$ reflecting the stress on the ocean surface due to winds. This model provides a simple way to produce interannual oscillations, and will be modified to produce irregular behavior below. We decompose the forcing into two parts, a seasonal component τ_s and a Walker circulation component τ_w . The latter stems from the increase in westward equatorial winds when the eastern Pacific is cool (η small), as was the basis for the model studied in Chap. 2. The wind stresses are given by

$$\tau_s = \tau_{0s}X(x)Y(y) \cos \omega t \quad (3.13)$$

$$\tau_w = \tau_{0w}X(x)Y(y), \quad \text{where} \quad (3.14)$$

$$X(x) = \cos \left[\frac{2\pi}{H} \left(x - \frac{L_x}{2} \right) \right], \quad \frac{L_x}{4} < x < \frac{3L_x}{4}, \quad (3.15)$$

$$Y(y) = \frac{1}{2} \left(1 + \cos \frac{2\pi y}{\lambda} \right), \quad |y| < \frac{\lambda}{2}, \quad (3.16)$$

$$X = Y = 0 \quad \text{otherwise.} \quad (3.17)$$

$\omega = 2\pi/\text{year}$, $\tau_{0s}=1.15\text{E-}5$ (m/s)², $\tau_{0w}=-5.0\text{E-}5$ (m/s)², and $\lambda=3000$ km. Physically, the total depth $h \equiv H + \eta$ measures the distance from the ocean's surface to the thermocline. h_e is the thermocline depth at the eastern boundary, measured along the equator two x -grid points from the boundary. The wind stress depends on h_e through a simple switching mechanism:

$$\tau^x = \begin{cases} \tau_b + \tau_s + \tau_w, & h_e < h_c, \\ \tau_b + \tau_s, & h_e \geq h_c \end{cases} \quad (3.18)$$

We call this the switched forcing model, or the SFM.

τ_b represents a background wind stress and is 0 for now. Fig. 3.3 shows a contour plot of the wind stress over our model ocean. Note that the only stress is in the zonal direction. Meridional winds are generally deemed unimportant in equatorial ocean dynamics, namely because they do not generate Rossby or Kelvin waves. h_c switches the Walker winds on and off, and is computed from the h_e to which the ocean relaxes in the absence of τ_s . Under these conditions, the ocean settles into a steady state known as Sverdrup balance [15]. Consider the SWM with steady flow, or $u_t = v_t = \eta_t = 0$. For our values of ν_h , ν , and κ , the friction and damping terms are small

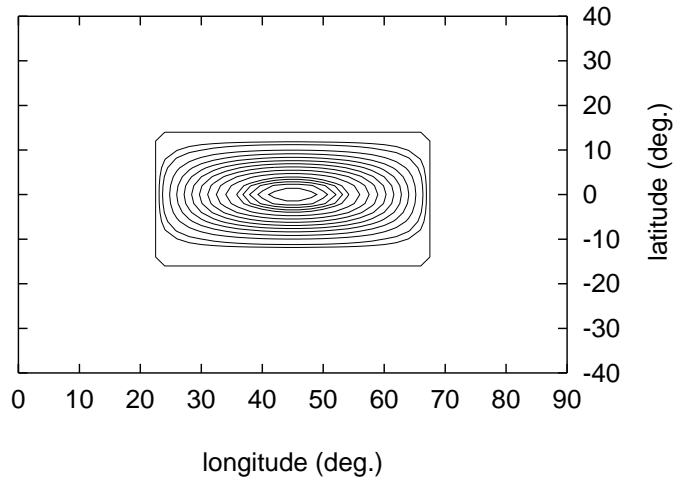


Figure 3.3: Contour plot of wind stress $X(x)Y(y)$.

compared to the Coriolis term and are for the moment neglected. We can now differentiate and combine Eqs. 3.1a and 3.1b to solve for v :

$$v = \frac{\tau_x^y - \tau_y^x}{\beta H}. \quad (3.19)$$

$y=0$ along the equator, so the right-hand side is 0 for τ_w given in Eq. 3.13. Eq. 3.1a and the boundary condition $u=0$ at the walls implies that $u=0$ on the equator. Eq. 3.1c then yields

$$\eta_x = \frac{\tau^x}{g'H}. \quad (3.20)$$

When a constant wind stress is applied, the ocean relaxes back to a state of no zonal flow once the transients die out. A constant pressure gradient (recall that η measures pressure in hydrostatic balance) matches the wind stress but drives no zonal current.

We define the value to which h_e settles when the ocean is forced by a constant stress τ_w to be h_w . We determine its numerical value by running the model until h_e appears to be constant. Fig. 3.4a shows h_e equilibrating in a 6-year integration; h_e continued its steady behavior when the model was run longer. We therefore let $h_w = h_e(10 \text{ years})$. The westward wind moves surface water to the west, generating east-moving Kelvin waves with $\eta < 0$ and west-moving Rossby waves with $\eta > 0$ (similar to Fig. 3.2). This leads to the minimum in h_e near 140 days. The waves reflect back toward the center from the coasts (the model has solid walls) and reach each other. As the winds

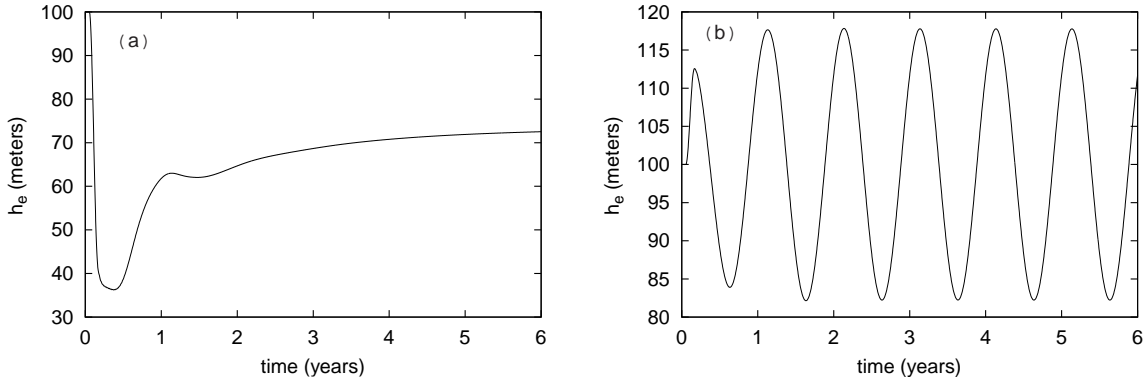


Figure 3.4: h_e for (a) Walker wind stress $\tau^x = \tau_w$, (b) seasonal wind stress $\tau^x = \tau_s$.

τ_b , (m/s) ²	h_w , m	Δh , m	h_a , m	h_c , m	h_b , m
0	73.4	17.9	82.1	86.7	91.3
$\tau_{b_1} = -3E-6$	66.1	17.9	82.1	83.0	84.0
$\tau_{b_2} = -6E-6$	58.8	17.9	82.1	79.4	76.7

Table 3.2: Values of switching parameters for various background westward winds τ_b .

generate new waves, the ocean eventually equilibrates to Sverdrup balance. McCreary showed that a necessary and sufficient condition for the model with seasonal forcing as in Eq. 3.18 to oscillate is

$$H - \Delta h = h_a < h_c < h_b = h_w + \Delta h, \quad (3.21)$$

where Δh is the amplitude of h_e oscillations due solely to τ_s [1]. As we see in Fig. 3.4b, the transients decay in the seasonally forced system within one year, after which time the system behaves periodically. We follow McCreary and let $h_c = (h_w + H)/2$, so that the inequality 3.21 is satisfied. Table 3.2 contains the numerical values of the relevant parameters for different choices of τ_b .

Fig. 3.5a shows the SFM oscillates between two equilibria, based on whether h_e is less than or greater than h_c . We have seen that the model equilibrates to Sverdrup balance when forced by τ_w alone; it is also clear that in the state of no forcing friction will make the ocean settle to a rest state. The seasonal forcing τ_s prevents the ocean from ever reaching either of these two states. For a detailed discussion, see [1]. A principal feature of the SFM which differs from the real El Niño is that it behaves periodically after the first time the switch is thrown. We see that this forcing scheme reproduces some of the hallmarks of El Niño, namely oscillations between a warm and cold phase

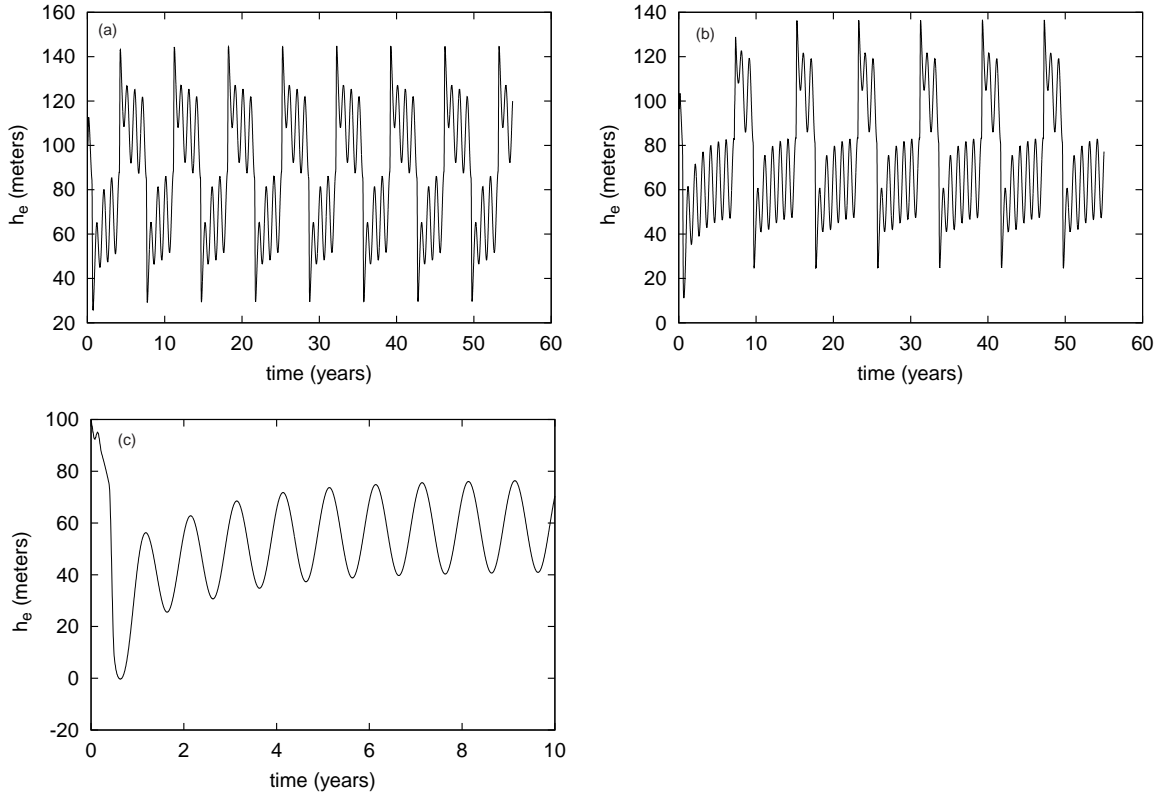


Figure 3.5: Evolution of SFM, $\tau_b =$ (a) 0, (b) τ_{b1} , (c) τ_{b2} . In each plot, h_c is the one for the appropriate τ_b from table 3.2. Model with τ_{b1} and $h_c=86.7$ m behaves like (c).

at an interannual period without ever equilibrating, but fails to capture the system's irregularity or cold-warm asymmetry.

A physical-motivated way to recover the observed asymmetry between cold and warm phases is to include a background westward trade wind, as we did with x^* in Chap. 2. We do this by adding a constant τ_b to every point within 10° of the equator. We then determine h_c as before, first by running the model with just τ_w and τ_b until Sverdrup balance is established. The resulting time series for h_e is qualitatively the same as for $\tau_b=0$, except that the minimum and equilibrium values are lower. When run with the seasonal forcing τ_s and τ_b , h_e is sinusoidal after some transients in the first year, as before. The amplitude of oscillation is the same, but the zero-point is shifted downward. With τ_{b_1} , the values in table 3.2 show the inequality 3.21 is still satisfied, and that h_c is roughly in the middle of h_a and h_b . However, we see in Fig. 3.5b that the cold phases are now longer than the warm ones. Although the lower h_c allows a smaller h_e to throw the switch, the eastern thermocline elevation due to τ_b overcompensates. The model still behaves periodically but has more pronounced transients than the $\tau_b=0$ case does (e.g., the first warm peak is lower than the later ones). In addition, the oscillation inequality is not met if we use the h_c we found for $\tau_b = 0$. Another way to prevent oscillation is to use a stronger τ_b so that the forcing never switches, such as $\tau_{b_2}=6\text{E-}6 \text{ (m/s)}^2$ (see Fig. 3.5c).

3.4 A More Realistic Forcing Function (CTM)

Although simple to implement and understand, the SFM discussed above has some unphysical aspects. First, the winds change discontinuously when $h_e = h_c$. A more specific drawback is that the forcing tends to leave physical bounds, and can produce an effect called outcropping of the layer. A more serious drawback to El Niño studies is that it is periodic, unlike the irregular real system. For these reasons, we also consider the smooth forcing

$$\tau^x = D(\hat{\eta})\tau_w + \tau_s + \tau_b, \quad \hat{\eta} \equiv \frac{-\bar{\eta}}{H}, \quad (3.22)$$

where

$$D(\hat{\eta}) \equiv \begin{cases} b_+ + \frac{1}{a_+} \left(\tanh \left[\frac{\kappa a_+}{b_+} (\hat{\eta} - \eta_+) \right] - 1 \right), & \hat{\eta} > \eta_+, \\ \kappa \hat{\eta}, & \eta_- \leq \hat{\eta} \leq \eta_+, \\ -b_- - \frac{1}{a_-} \left(\tanh \left[\frac{\kappa a_-}{b_-} (\hat{\eta} - \eta_-) \right] - 1 \right), & \hat{\eta} < \eta_- \end{cases} \quad (3.23)$$

$\bar{\eta}$ is the average η within 6° longitude from the eastern wall and 3° latitude from the equator, weighted by a grid point's area (we are on a spherical geometry). For $D(\hat{\eta})$ to be continuous, we must have $a_\pm > 0$ and

$$\eta_+ = \frac{b_+}{\kappa} \left(1 - \frac{1}{a_+} \right), \quad \eta_- = \frac{-b_-}{\kappa} \left(1 - \frac{1}{a_-} \right). \quad (3.24)$$

a_\pm measures the curvature of D , b_\pm are the values D approaches away from $\hat{\eta}=0$, and κ is the slope of D at 0. $D(\hat{\eta})$ was presented as a reasonable forcing function in [3], and the form Eq. 3.22 was suggested in a study of basin size effects on El Niño [12]. This function turns the Walker circulation on and off gradually. We define $\hat{\eta}$ with a negative sign so that $D(\hat{\eta})$ mimics McCreary's switching and turns on for an elevated thermocline ($\eta < 0$). A nonzero b_- causes the Walker cell to run in reverse for $\hat{\eta} > 0$. We call this system the continuous tanh model, or CTM. It is possible to center D on h_c rather than H, but we do not investigate that approach here.

Since a full exploration of reasonable parameters for D is computationally prohibitive, we follow [3] and set $a_+=3$, $a_-=1$, $b_+=1$, and $b_-=0.5$ and vary κ . Fig. 3.6 presents D for these values and $\kappa=1.75$, and Fig. 3.7 plots the model's behavior for various κ . Three generic behaviors occur, depending on κ . For $\kappa=1.5$ or smaller, the system behaves like a driven, slightly damped oscillator. There are some minor transients that quickly give way to an annually-periodic solution. $\kappa=2$ leads to a large separation between the warm and cold states, with the system switching every few years between the two. After a longer period of transient behavior, the system becomes periodic. This approximates the behavior of the SFM's step function coupling of the Walker stress, which is $D(\hat{\eta})$ (centered on h_c) in the limit of infinite κ and $b_-=0$. $\kappa=1.75$ and 1.9 seem to be a happy medium between these two regimes, with neither the seasonal nor Walker forcing dominant.

We can recapture the warm-cold asymmetry and produce more irregularity with a background wind τ_b as above. Fig. 3.8a displays h_e over time for $\kappa=1.9$ and τ_{b_2} , twice the background wind used in the switched model above. One should think of El Niño as peaks with anomalously deep thermoclines rather than simply as those years where the thermocline is below the mean depth

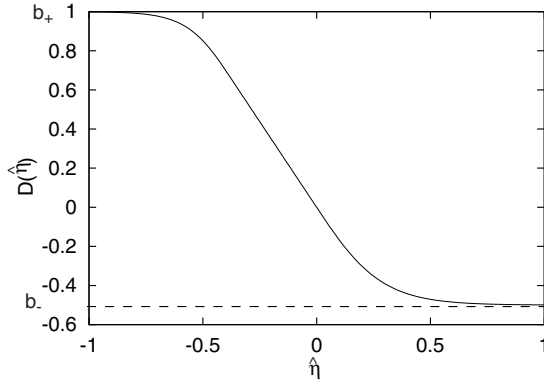


Figure 3.6: Coupling function $D(\hat{\eta})$ for $\kappa=1.75$.

$H=100$ m. Although the system acts more or less periodically (some residual transient behavior remains), the period is interannual (about 6 years) and contains a nontrivial structure (one sharp El Niño peak, extrema at different h_e values). This model will be useful for studying the effects of westerly wind events in Chap. 4. In addition, the system can be made irregular by dropping τ_b off gradually. We do this by setting τ_b to τ_{b_2} within 8° of the equator, $\tau_{b_1}(=\tau_{b_2}/2)$ 10° from the equator, and 0 elsewhere. Fig. 3.8b was produced using this nonuniform background wind. This model was run for 1000 years and never settled into a clearly periodic behavior, indicating that the variability is not simply transient. There are some clear patterns in the plotted signal, but the changing heights of analogous peaks and the lull near year 925 attest to the aperiodicity.

Analyzing this run reveals further agreement with basic El Niño properties. We define an El Niño to be a maximum in $h_e > 110$ m that occurs at least 1 year after another such maximum (we count 2-peaked events as one event). This leads to 248 events in 1000 years, which is reasonable for the real system. We define event time as the time of maximum h_e . Fig. 3.9a is a histogram of time between successive events, showing they occur interannually but not at a set interval. As in the real system, Fig. 3.9b shows a trend for stronger El Niños to be followed by longer stretches of a cold eastern Pacific. In addition, Fig. 3.10 reveals a strong coupling of event onset to the time of year when the seasonal trades τ_s are their most westerly ($\cos(\omega 0.5)=-1$). This agrees both with nature and the seasonal x^* from Chap. 2. The deterministic ODE system presented there recovers certain broad aspects of the El Niño through chaos, but grossly simplifies the ocean to two grid points. The nonuniform wind forcing discussed here treats the full spatial structure of the ocean through the PDE shallow-water model, and still recovers El Niño behavior without using stochasticity. Finding

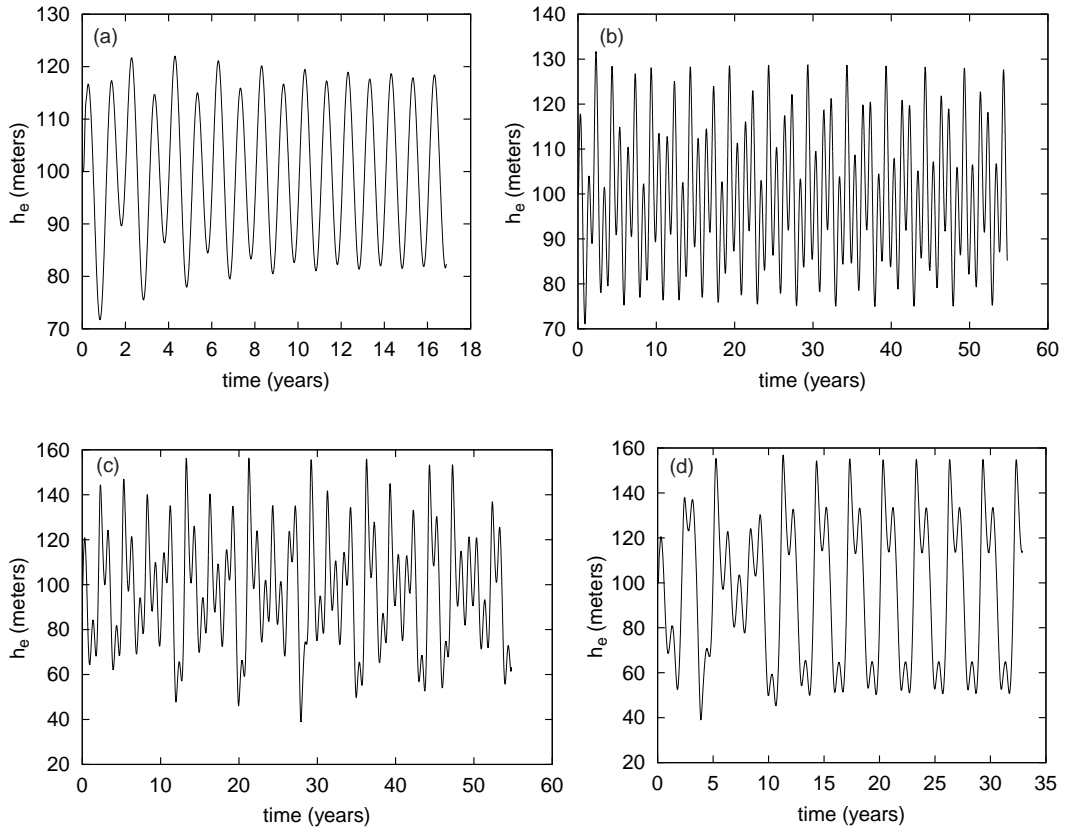


Figure 3.7: h_e for CTM, $\tau_b=0$, $\kappa =$ (a)1.5, (b)1.75, (c) 1.9, (d) 2.0.

the right wind structure was crucial in generating interannual and irregular motion, with the ocean dynamics being kept the same throughout this chapter.

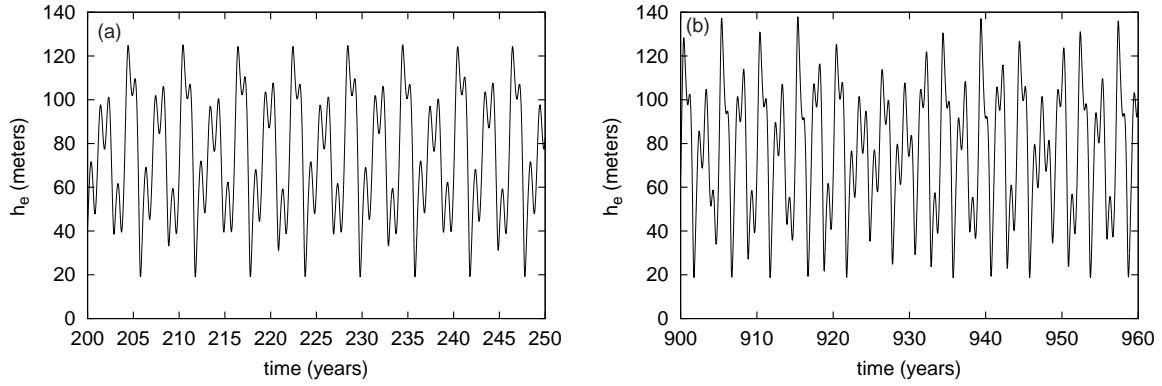


Figure 3.8: h_e for CTM, $\kappa=1.9$. (a) uniform τ_{b_2} produces interannual but periodic behavior. (b) nonuniform τ_b (τ_{b_2} , dropping to τ_{b_1} , then 0) produces some variability even after 900 years.

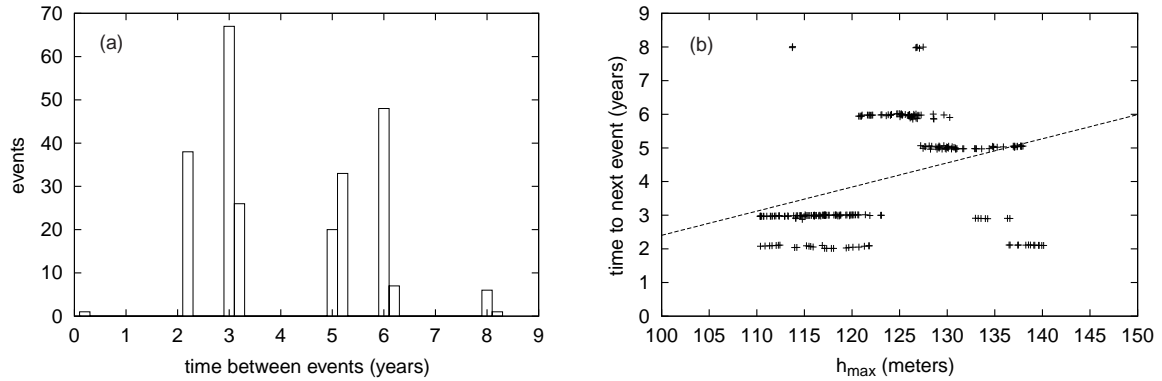


Figure 3.9: (a) Histogram of time between El Niño events. (b) Time before next event vs. h_e of peak, with best-fit line showing increased lag after strong events.

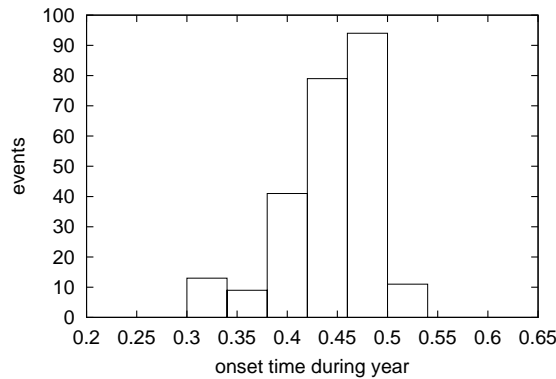


Figure 3.10: Histogram of onset time during year. Indicates very strong coupling to time of maximum (most eastward) τ_s .

Chapter 4

Noise and Westerly Wind Events

This chapter explores the effects of stochastic wind noise and westerly wind events on the models developed in Chap. 3. The SFM is quite sensitive to noise that moves h_e across h_c , and even weak noise can push solutions permanently out of phase with the noiseless one. Noise can also have a large effect on the CTM, but it does not have the same critical dependence on h_e of the SFM. Westerly wind events can generate significant transients in the CTM for several years, after which the ocean may return to its unperturbed, periodic behavior or be permanently different. This is consistent with treating h_e as a damped, driven oscillator, with the wind events acting as impulsive forces that generate transients. In addition, wind events prove insufficient to immediately trigger an El Niño in the CTM, and have only a small immediate impact on the ocean. The SFM, on the other hand, is very quickly thrown into an El Niño state by wind events, demonstrating that the role of these events in El Niño onset may depend strongly on how sensitive the Walker circulation is to the eastern thermocline.

4.1 Stochastic Noise in the Wind Field

A major source of stochasticity in the ocean-atmosphere system is the ever-present, local wind fluctuations that we have no hope of resolving with our model. We add such wind noise via the

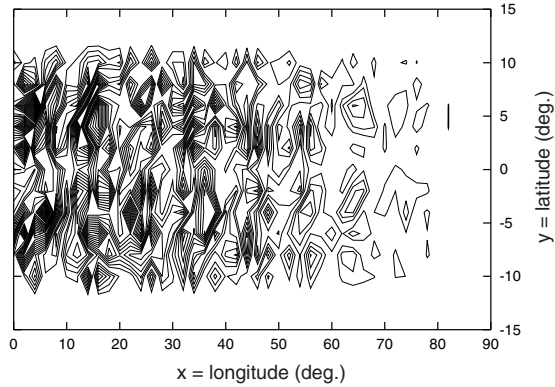


Figure 4.1: Contour plot of noise, showing eastward decline and sine-induced spatial structure.

following formula:

$$N(x, y, t) = A(x, y, t) (1 + |\sin(k_x x)|) (1 + |\sin(k_y y)|) b \left(1 - \frac{x}{x_e}\right), \quad (4.1)$$

$$A(x, y, t_{i+1}) = \lambda A(x, y, t_i) + r(x, y, t_i) A_N \sqrt{1 - \lambda^2}. \quad (4.2)$$

We compute N once a day and add it to the calculated τ^x at every point within 10° latitude of the equator. We choose this form so that the noise is non-white both over time and space. The sine terms provide some structure over scales typical of weather events, with $k_{x,y}$ corresponding to wavelengths of 20° . The linear part reflects the fact that storms tend to be stronger in the western Pacific. x_e is the longitude of the eastern ocean boundary, making the linear part b at the western end ($x=0$) and 0 at the eastern ($x=x_e$). The value of λ determines how quickly $N(x, y)$ decorrelates from its prior values, and matches the noise scheme from Chap. 2. $\lambda=0$ corresponds to white noise over time at a single grid point. As before, let us choose λ so that a disturbance will decay by 99% in 15 days, giving $\lambda=0.74$. $r(x, y, t_i)$ is a random number uniformly distributed between -1 and 1, and is different for each grid point. Fig. 4.1 displays a contour plot of the wind noise on some day. For convenience we do not include any noise in the meridional winds τ^y , because most studies indicate this noise to be smaller in amplitude and unimportant to equatorial ocean dynamics. For example, [10] found the optimal wind noise for promoting variance growth (a measure of how divergent two solutions are) in a coupled ocean-atmosphere model used to predict El Niño has very small meridional components.

We set an amplitude A_N for the wind noise by comparison with the seasonal wind stress. It is

generally accepted that the noise amplitude is roughly the same strength as the seasonal component and can be stronger at some times. When $t=0$ (i.e., $\cos(\omega t)=1$ in Eq. 3.13), the average τ_s over the region where it is nonzero is 3.4 in arbitrary units. Fixing $b=0.2$, a value of $A_N=0.001$ gives an average noise stress amplitude of 3.7 over the region where it is applied. Running the $\tau_b=0$ SFM with noise of this strength produces a different solution from the unperturbed case, as is shown in Fig. 4.2. Notice that h_e departs very little from its unperturbed value with this wind noise, indicating just how sensitive the model is to any crossing of $h_e = h_c$: this prematurely switches the Walker forcing. This is much more likely to happen when h_e is at an annual maximum, which is what we observe. As a result, onset of El Niño, or a warm ocean, is quite strongly coupled to the seasonal cycle. Since the warm phase is not affected, we have recovered a warm-cold asymmetry. The fact that noise shortens the cold intervals most likely depends on whether the warm or cold annual peaks are closer to h_c ; it is entirely conceivable that the warm phase would be contracted in a model with slightly different parameters, a physical reason to adopt a larger h_c , or a westward background wind τ_b . Fig. 4.4 displays the area-weighted average absolute value of the difference between η of the noiseless (a) and noisy (d) models within 10° of the equator over the entire zonal extent, normalized by the total fluid depth H (referred to as AED). From this, we see that the ocean on a large scale is in a different state when h_e is in a warm rather than cold state.

Fig. 4.2 also reveals that both the western and eastern noise are important to switching the ocean state. N is calculated as above but only applied in the eastern half of the ocean for (b) and the western half for (c). Both of these schemes are capable of switching the ocean, sometimes in different years. Noise in the west affects the eastern thermocline by generating east-moving Kelvin waves. When noise is applied everywhere as in (d), there are times when both the western and eastern noise are necessary to change state. An ocean that is switched by noise is permanently out of phase with an unperturbed one, as Fig. 4.3 shows. Here, noise is applied for the first 17 years and then turned off. Note, however, that once the noise is removed, the model behaves exactly as the unperturbed one does, just shifted in time.

Wind noise affects the CTM differently than it does the SFM. Fig. 4.5a shows how the CTM behaves with $A_N=0.004$ noise applied over the whole ocean, and (b) depicts the AED between this run and one without noise. We set $\kappa=1.9$ and $\tau_b=0$, the same settings that were used for Fig. 3.7c. The model was first run for 15 years to reduce transient behavior, noise was applied for 25 years,

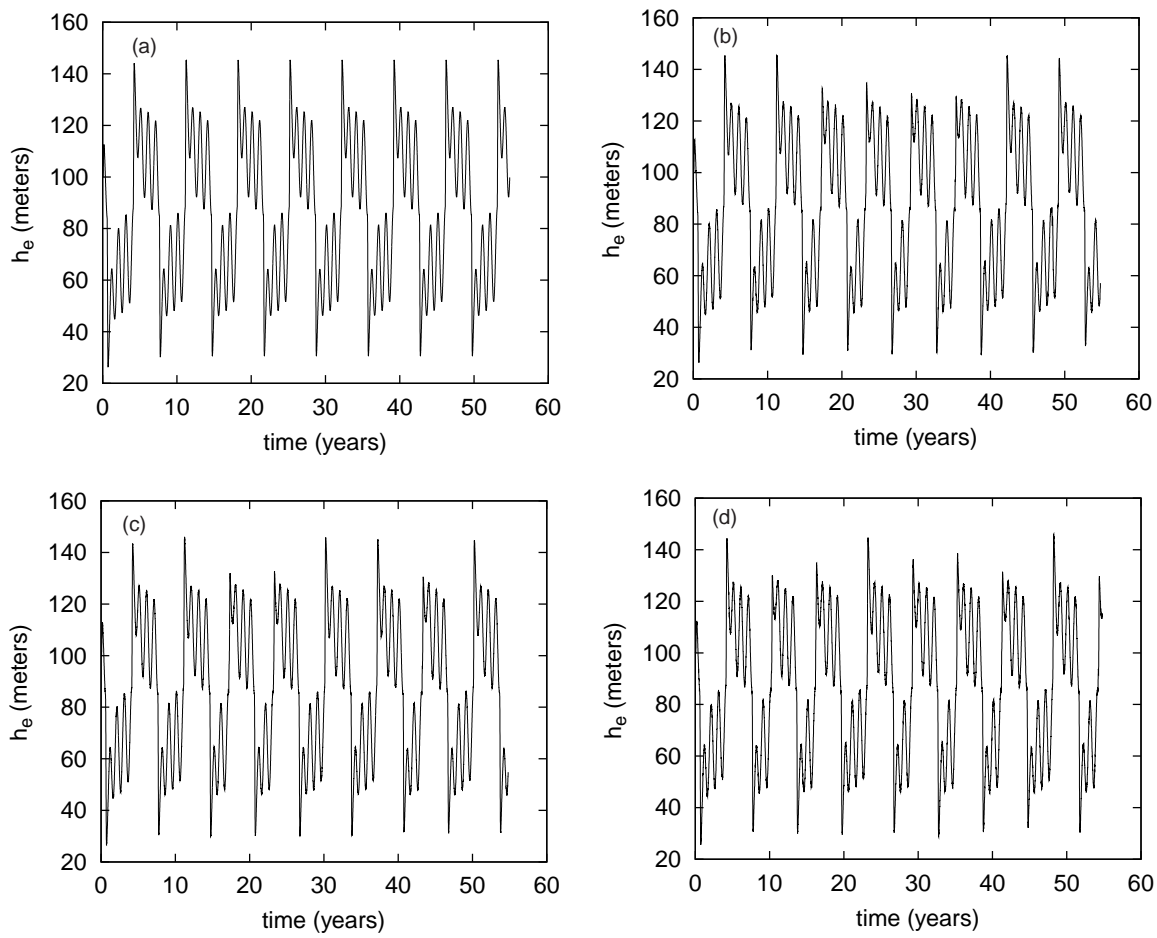


Figure 4.2: $\tau_b=0$ SFM with noise strength $A_N=0.001$ applied (a) nowhere, (b) the eastern ocean, (c) the western ocean, and (d) everywhere.

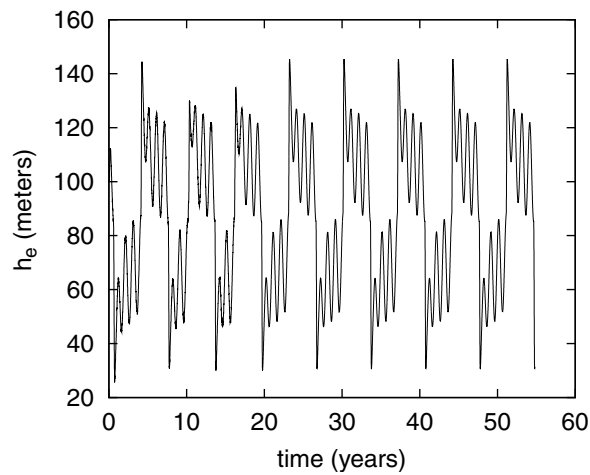


Figure 4.3: $\tau_b=0$ SFM with $A_N=0.001$ noise applied to whole ocean for first 17 years.

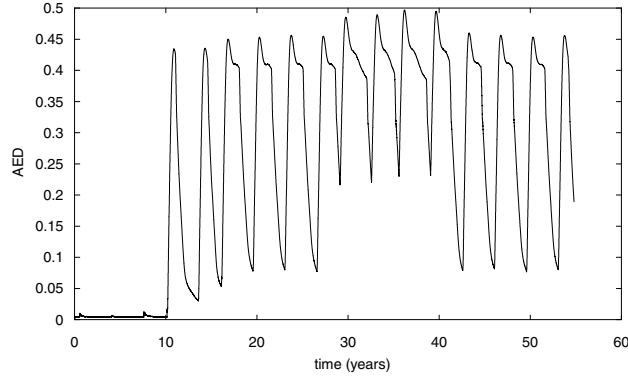


Figure 4.4: Average η difference AED for SFM with and without noise over whole ocean.

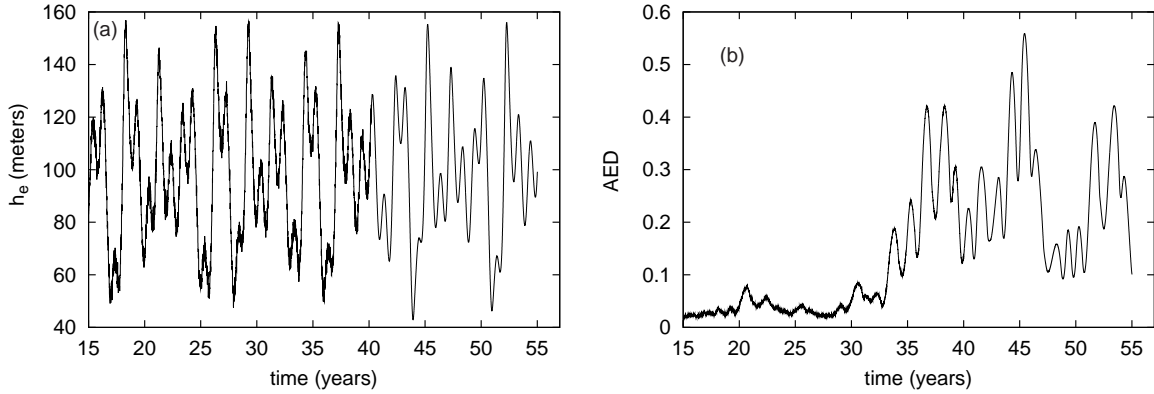


Figure 4.5: Continuous coupling for $A_N=4E-3$. (a) h_e for model with noise, (b) AED.

and was then turned off for the next 15 years. Although the value of A_N used above (0.001) also significantly perturbs the model, we choose 0.004 to show that the CTM is more resistant to noise. While noise throws the SFM into a different state as soon as h_e approaches h_c , the stronger noise used for the CTM run took 18 years to do this even though h_e was moving between warm and cold phases. The response to noise indicates that the CTM does not share the sensitive dependence on h_e present in the SFM, which one would not expect in a large, massive system like the ocean. Both of the SWM-based models contrast sharply with the chaotic model of Chap. 2, where miniscule noise very quickly drives solutions apart. Moreover, the perturbed ocean does not seem to merely be a shifted version of the unperturbed one after we turn the noise off. The qualitative features (aperiodicity, interannual oscillations) of the two time series for h_e nonetheless agree.

4.2 Effects of Westerly Wind Events

A topic of recent interest in El Niño studies has been the connection with westerly wind events (WWEs). The term refers to short-term (~ 10 days) atmospheric events over the western or central Pacific with eastward-blowing (westerly) winds that are significantly stronger than typical winds. Overall properties of the WWEs for the 1986-1995 period are presented in [9]. Harrison and Vecchi classify WWEs into eight groups, based on the location of the maximum wind anomaly from a climatological background. They produce composite events by averaging the winds of all the events in a given category. The distance these events translate during their lives is generally much smaller than their spatial extent, and they tend to move in the zonal direction. They also find that the zonal structure of WWEs are well-fitted by the gaussian

$$u(x, y, t) = u_0 \exp \left[- \left(\frac{x - x_0 + c_x t}{L_x} \right)^2 - \left(\frac{y - y_0 + c_y t}{L_y} \right)^2 - \left(\frac{t}{T} \right)^2 \right]. \quad (4.3)$$

x_0 and y_0 are the coordinates of the event center, which moves with speed (c_x, c_y) . We use this formula for the wind field strength instead of composite data sets. The only major difference from the measured wind field is the lack of any meridional winds. But, as discussed above, they are not considered important in equatorial ocean dynamics.

As is typical of the wind stresses we have explored, WWEs generate Rossby and Kelvin waves analogous to the ones seen in Fig. 3.2. The westerly wind pushes warm surface water eastward, thereby depressing the eastern thermocline. The east-moving Kelvin wave therefore consists of a positive surface displacement, while the west-moving Rossby waves have $\eta < 0$. Since the eastern thermocline controls the wind stress on the ocean, WWEs can interact with the El Niño cycle. The observed connection of WWEs with El Niño is most strongly seen in the Southern Oscillation Index (SOI), usually taken as the pressure difference between Tahiti and Darwin, Australia. Harrison and Vecchi found strong lagged correlations between WWEs of a particular type and the SOI. The category with the statistically most significant correlation was the central (C) events at no lag, so we choose to investigate it. In particular, C events tend to occur during El Niño events, which correspond to a negative SOI.

C events are centered on the equator at 170° E longitude, and will be placed near the western

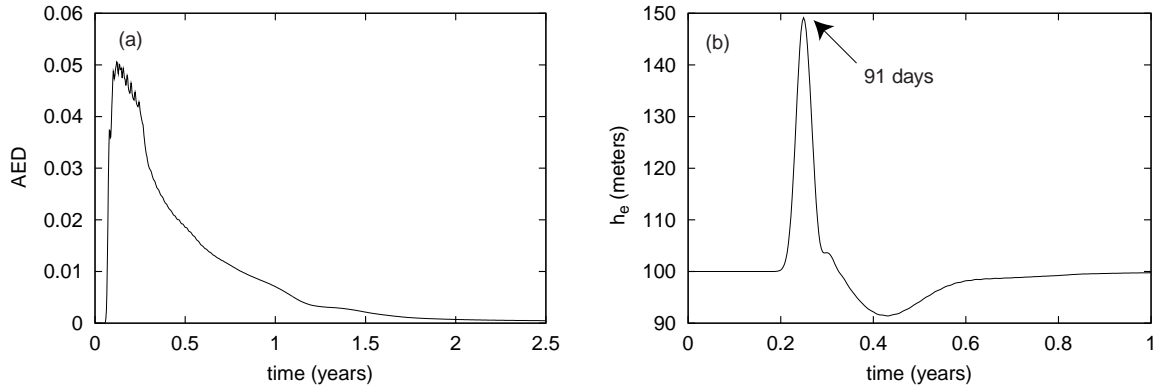


Figure 4.6: (a) AED between windless models with and without a C event. (b) h_e with C event.

edge of our model. Since the real Pacific is larger than the ocean we have been using, we only apply the event within $L_x/2$ and L_y of the center. The best-fit parameter values for this type are $u_0=6.4$ m/s, $L_x=16.2^\circ$, $L_y=5.4^\circ$, $T=3$ days, and $c_x=c_y=0$. We apply the event for 12 days, twice the temporal e -folding time before and after $t=0$. To apply the event, we add the wind calculated via Eq. 4.3 to what the wind stress would otherwise be. We need to convert atmospheric wind speeds to ocean forcings τ^x . A value of $\gamma=5\text{E-}5/\text{s}$ is calculated in [16] using basic thermodynamic arguments and is adopted here. This leads to an peak event stress of $3\text{E-}4$ (m/s)², which is much higher than τ_{0_s} and τ_{0_w} . Fig. 4.6a displays the AED between a steady, unforced ocean and one which has experienced a C event on day 20. This shows that an event can have a minor effect on the ocean, but decays to an insignificant level after 2 years. We can also see from the plot of h_e in Fig. 4.6b that the east-moving Kelvin wave possesses a positive η , and allows us to estimate the lag between event onset and when the wave reaches the eastern boundary. The maximum h_e occurs at 91 days, or 65 days ($91-20+6$) after the maximum winds of the event. This is in excellent agreement with the Kelvin wave theory worked out above: to travel from 17° to 86° at speed $c = \sqrt{g'H} = 1.41$ m/s takes 63.5 days.

We now apply C events to a CTM ocean with $\tau_b=\tau_{b_2}$ and $\kappa=1.9$, corresponding to Fig. 3.8a. In broad terms, we see that h_e acts like a damped, driven oscillator: the event can be thought of as an impulsive forcing, which generates transients. Fig. 4.7 displays four oceans with a C event applied at varying times. Runs with events applied at other times agree with the following discussion. In general, the event does not produce a significant change in the ocean state for at least a year after it happens. h_e evolves in the short term almost exactly as it otherwise would; in particular, WWEs

do not appear to trigger an El Niño event. We see this whether the event reaches the eastern boundary during a crest, a trough, or somewhere in between. However, events can produce large deviations in ocean behavior on the scale of several years, and even seem able to move the ocean into a permanently different regime. The first way is by making the interannual, periodic cycle more regular. In panel (c), for instance, the warm phases (large h_e) are all very similar after the event, while in the unperturbed ocean we see two distinct types of warm phases. Perhaps there is more than one stable periodic solution for h_e , and the event throws the model from one into another. The other possible permanent difference is a temporal phase shift. Panel (g) shows the ocean evolving basically as the unperturbed ocean does, except shifted in time.

The failure of WWEs to push the CTM ocean into an El Niño state stands in stark contrast to their effect on the SFM. We have already seen how sensitive the switched system is to the precise value of h_e : once it crosses h_c , the ocean changes state. Any spike large enough to do this (which for a model such as that in Fig. 3.5 almost all of them are) immediately prompts an El Niño. Both of these models contain identical ocean dynamics and differ only in the way the Walker wind stress couples to the eastern thermocline. The winds in the SFM change abruptly based solely on the value of h_e , while the CTM winds change gradually with the average η over a 6° by 6° patch. One therefore needs a stronger, more coherent disturbance of the eastern ocean in the CTM to drastically alter the ocean and trigger an El Niño. Recent studies that show wind events are able to cause El Niño utilize more sophisticated models than the ones used here; for instance, they may simulate a complete atmosphere governed by the SWM rather than simply a parametrized wind field, or the ocean may include active thermodynamics. As was mentioned in Chap. 3, running an ocean and atmosphere alongside each other produces disturbances that grow without bound in the course of several weeks. Perhaps models which capture more details of the ocean-atmosphere system contain small-scale positive feedback that allows little perturbations, such as those caused by a wind event, to grow into a full-blown El Niño.

We should be skeptical as to how well our westerly wind events replicate the effects of real ones. First, the spikes of tens of meters in h_e seem rather large for anything short of an extreme occurrence. This may be due to the value we use for the coupling parameter γ being out of proportion with our choice of friction and wind stress constants. It is unlikely that using a larger ocean will significantly reduce the spike height, since Kelvin and Rossby do not dissipate much. If

our simulated wind events are much stronger than their counterparts in nature, this should further convince us that these events do not have a major immediate effect on the CTM ocean (e.g., they cannot push the ocean into an El Niño).

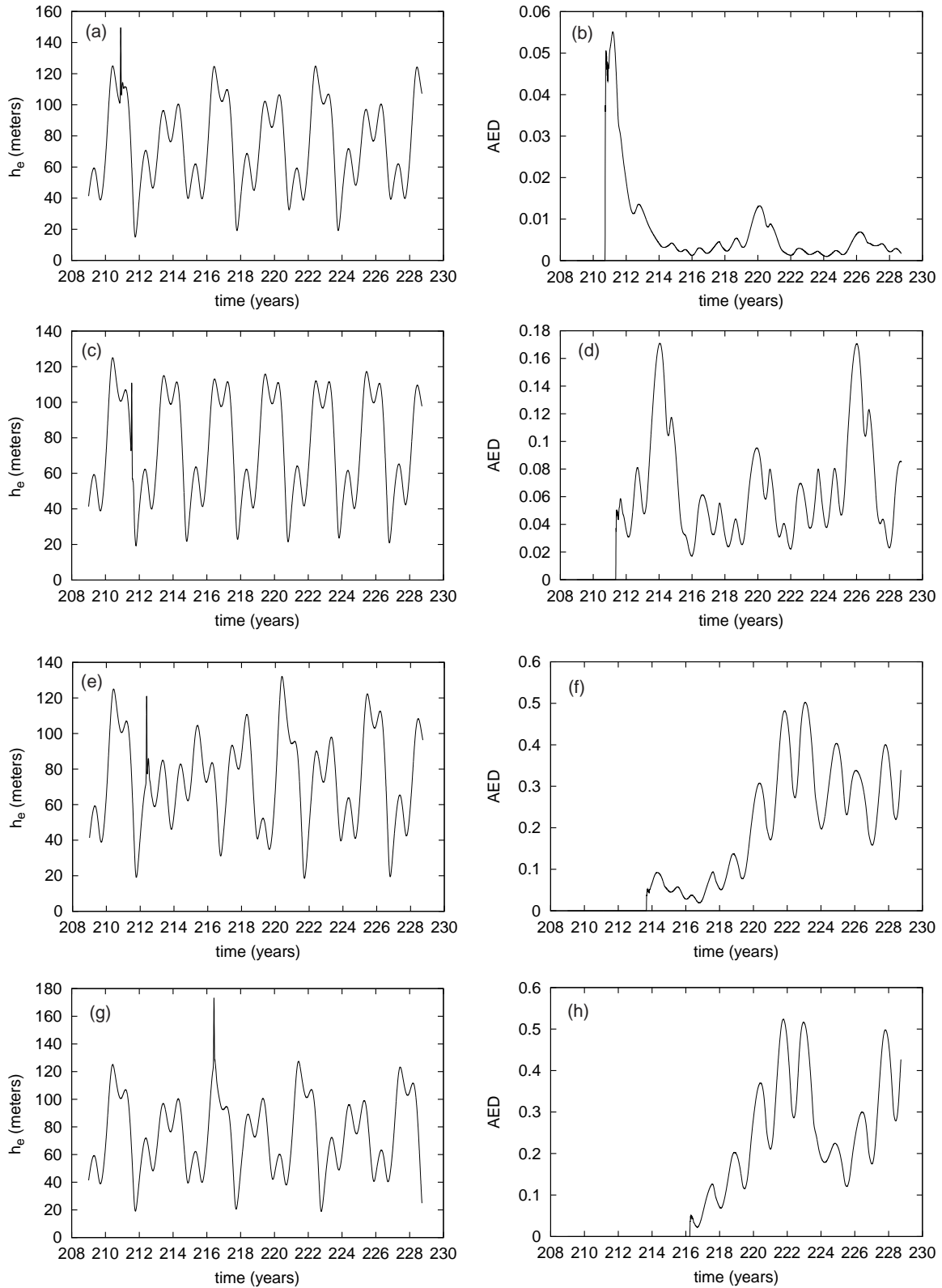


Figure 4.7: h_e and AED for C wind event applied at different times to CTM with $\kappa=1.9$, $\tau_b=\tau_{b_2}$. (a,b) event causes weak disturbance that dies, (c,d) model becomes more regular (difference between the two warm phases in unperturbed model disappears), (e,f) large disturbance occurs several years after event, (g,h) ocean approaches unperturbed behavior but is phase-shifted.

Chapter 5

Conclusions and Future Prospects

This thesis has explored a series of El Niño models that contain many basic aspects of the real system, namely interannual, irregular oscillations and phase-locking to the seasonal cycle. We have seen that simple, deterministic models reproduce these El Niño features, lending credence to the notion that El Niño arises from large-scale, basic physics of the tropical ocean-atmosphere system. We first considered a chaotic ODE model, and then proceeded to periodic PDE models. While these latter models resemble damped, driven oscillators rather than chaotic systems, a non-uniform wind field introduces irregular behavior. The basic El Niño-like aspects of these models persist under stochastic wind noise and westerly wind events, both of which add variability to the PDE systems. The basic ocean dynamics in all of these models is a simple linear shallow-water model with friction, and only the wind field or the way it depends on the state of the ocean were varied. This shows that changing the winds is sufficient to dramatically alter the behavior of a coupled ocean-atmosphere system, and that much of El Niño unpredictability may be due to detailed yet deterministic aspects of the atmosphere.

Chap. 2 showed how an ODE model based on large-scale ocean dynamics with intrinsic chaos can generate El Niño events. The system is quite similar to the Lorenz equations, and is chaotic for physically reasonable choices of parameters. The background westward wind x^* causes the eastern ocean to preferentially stay in the cold state and occasionally venture into a warm El Niño state. Including the seasonal cycle in x^* or the equilibrium temperature T^* partially phase-locks event onset to time of year, although we must increase the wind coupling B to maintain the warm-cold asymmetry. When we apply stochastic noise to the wind x , the model behaves qualitatively the

same as before even for relatively strong noise amplitudes. Since the model is chaotic, even a miniscule noise level causes solutions to rapidly diverge from the unperturbed case. This model provides a “proof of principle” that basic El Niño properties may be explicable by low-order physics, but it does not remain chaotic when we resolve space more finely. We can view the model as a two-point discretization of the PDE Eq. 2.2, but it becomes stable as we add more x grid points [23]. It is a fairly common property of chaotic, low-order ODE truncations of PDE systems that the chaos disappears as we include more modes.

We must reject as unphysical any aspects of an ocean model which do not persist merely as we increase the spatial resolution. Therefore, we explored models based on the shallow-water equations, a PDE system used extensively in the study of homogeneous geophysical fluids. The essential ocean dynamics in this model are equatorial west-moving Rossby and east-moving Kelvin waves. Instead of simulating a separate atmosphere and coupling it with the ocean, we parametrize the atmosphere as wind-induced body forces to the surface ocean currents. A switched forcing mechanism (SFM) oscillates interannually between a warm and cold state, and behaves asymmetrically when a background easterly wind τ_b similar to x^* is added. The SFM winds consist of a seasonal cycle with a Walker circulation turned on when the eastern thermocline h_e is above a critical depth h_c . Since this system is periodic and has a physically-unappealing discontinuous coupling of the Walker stress, we adopt a model with continuous coupling (the CTM). Here, h_e acts like a damped, driven oscillator, with transients that eventually decay and leave a periodic solution. For the appropriate values of κ (such as 1.75, 1.9), the model’s period is interannual and displays richer structure than SFM does. τ_b again makes the eastern ocean tend to be cold but does not make the model aperiodic. With nonuniform easterly wind (τ_{b_2} within 8° of the equator and τ_{b_1} at 10°), however, the model possesses significant irregularity against a periodic backdrop even after being run for 1000 years. This affects the height of h_e peaks which correspond warm states, giving us the hallmark variability of El Niño. We chose maxima in h_e greater than 110 m to represent events, and found very strong locking to the seasonal cycle and an increase in the time between two events with the strength of the first one. This model seems to conform with the widely-held view that ENSO is a perturbation to the annual cycle.

A crucial test of these PDE models’ utility is how they respond to stochastic forcing. We first applied random wind noise to the SFM, and found that noise both in the western and eastern

parts of the ocean sufficiently agitated h_e to throw the switch and change the large-scale state of the ocean. The extreme sensitivity to h_e is of course lost in the CTM, where noise is still able to significantly alter the ocean. This takes many years, however, which is consistent with viewing the model as a damped, driven oscillator rather than as a chaotic system. Westerly wind events are also able to cause large disruptions in the CTM ocean that last for several years, perhaps permanently phase-shifting the ocean. However, wind events are not able to affect the ocean state over the short term (<1 year), which argues against some recent speculation that these events could trigger El Niño oscillations. On the other hand, wind events lead instantly to El Niño events in the SFM, because η at one point (h_e) turns the Walker wind on and off. This suggests that an accurate picture of how the eastern thermocline interacts with the Walker circulation is essential to understanding the role of wind events in El Niño onset. Perhaps the instability present in systems with a complete rather than parametrized atmosphere allow the perturbations in h_e caused by wind events to grow quickly enough to induce an El Niño in a model like the CTM, where the Walker cell turns on and off gradually based on a spatially-averaged η .

There are currently a number of possible mechanisms for explaining the interannual, aperiodic nature of El Niño. Intrinsic chaos is one approach. While the ODE model from Chap. 2 is chaotic, the only PDE model considered here that may possess chaos in h_e is the CTM with nonuniform τ_b . It is daunting to analytically investigate the properties of a single grid point in a PDE model, but numerical studies of stability, Lyapunov exponents, and other tools of dynamical systems can illuminate the nature of the irregularity in this system. Another way to add variability to the periodic PDE systems is through long-term changes in parameters such as κ . For instance, it is believed that midlatitude ocean dynamics change internally on the scale of decades, and that weather events can propagate these changes to the lower latitudes. Since CTM is a damped, driven oscillator, varying parameters can constantly generate transients that last for several years, and mask the system's underlying periodicity. Besides deterministic processes, we have also seen that CTM is susceptible to large-scale perturbation from wind noise and westerly wind events. Although these disturbances do not seem to promote El Niño, they do lead to irregularity. Any workable model must at least behave qualitatively like the El Niño in the presence of noise and wind events, since they are indeed present in nature. All of the models presented in the thesis do this, which further encourages us that they capture some of the physics essential to El Niño.

There is currently a very active debate about what parts chaos, deterministic processes, and stochasticity play in El Niño, and we can hardly claim to have settled this complex issue here. This discussion serves to illustrate the general nature of geophysical research. No one doubts that we know the underlying physics of fluid flow and rotating reference frames. The problem, however, lies in making the appropriate simplifications that retain the needed physics while still being tractable. Moreover, there is a scarcity of detailed empirical data about the ocean-atmosphere system, and (fortunately for living organisms) we lack the ability to conduct anything like a controlled experiment on geophysical scales. Ocean science involves a good measure of art, in choosing what aspects of the system to neglect and emphasize in a given situation. The perverse ability of intermediate models to outperform the most sophisticated general circulation models in El Niño predictions affirms that bigger computers, smaller grid spacing, and greater numerical precision does not guarantee a better understanding of nature. Many oysters concealing pearls of wisdom still reside under the sea, waiting not just for the sledgehammer of supercomputers but also for the delicate touch of theoretical physicists.

Bibliography

- [1] D. L. T. Anderson and J. P. McCreary. A simple model of El Niño and the southern oscillation. *Monthly Weather Review*, 112:934, 1984.
- [2] W. E. Boyce and R. C. DiPrima. *Elementary Differential Equations and Boundary Value Problems*. Prentice-Hall, Inc, sixth edition, 1997.
- [3] M. A. Cane, M. Münnich, and S. E. Zebiak. A study of self-excited oscillations of the tropical ocean-atmosphere system. Part II: Nonlinear cases. *Journal of the Atmospheric Sciences*, 48:1238–1248, 1991.
- [4] M. A. Cane and S. E. Zebiak. A model El Niño-southern oscillation. *Monthly Weather Review*, 115:2262–2278, 1987.
- [5] B. Cushman-Roisin. *Introduction to Geophysical Fluid Dynamics*. Prentice-Hall, Inc, 1994.
- [6] D. B. Enfield. El Niño, past and present. *Reviews of Geophysics*, 27:159, 1989.
- [7] John Guckenheimer and Philip Holmes. *Nonlinear Oscillations, Dynamical Systems, and Bifurcations of Vector Fields*. Springer-Verlag, 1983.
- [8] G. J. Haltiner and R. T. Williams. *Numerical Prediction and Dynamic Meteorology*. Wiley, second edition, 1980.
- [9] D. E. Harrison and G. A. Vecchi. Westerly wind events in the tropical Pacific, 1986-1995. *Journal of Climate*, 10:3131, 1997.
- [10] R. Kleeman and A. M. Moore. A theory for the limitation of ENSO predictability due to stochastic atmospheric transients. *Journal of the Atmospheric Sciences*, 54:753, 1997.

- [11] J. B. Marion and S. T. Thornton. *Classical Dynamics of Particles and Systems*. Harcourt Brace & Company, fourth edition, 1995.
- [12] Linda Metaxas. Private communication.
- [13] J. D. Neelin, D. S. Battisti, et al. ENSO theory. *Journal of Geophysical Research*, 103:14, 1998.
- [14] R. C. Pacanowski. Private communication.
- [15] S. G. H. Philander. *El Niño, La Niña, and the Southern Oscillation*. Academic press, Inc, 1990.
- [16] S. G. H. Philander, T. Yamagata, and R. C. Pacanowski. Unstable air-sea interactions in the tropics. *Journal of the Atmospheric Sciences*, 41:604, 1984.
- [17] P. Pokorny. *EASYNUM*. 1995.
- [18] W. Press, S. Teukolsky, W. Vetterling, and B. Flannery. *Numerical Recipes in C*. Cambridge University Press, second edition, 1992.
- [19] R. Sadourny. Compressible model flows on the sphere. *Journal of the Atmospheric Sciences*, 32:2103, 1975.
- [20] R. Sadourny. The dynamics of finite-difference models of the shallow-water equations. *Journal of the Atmospheric Sciences*, 32:680, 1975.
- [21] M. J. Suarez and P. S. Schopf. A delayed action oscillator for ENSO. *Journal of the Atmospheric Sciences*, 45:3283, 1988.
- [22] G. K. Vallis. El Niño: A chaotic dynamical system? *Science*, 232:243, 1986.
- [23] G. K. Vallis. Conceptual models of El Niño and the southern oscillation. *Journal of Geophysical Research*, 93:13, 1988.